Monthly Notices of the ROYAL ASTRONOMICAL SOCIETY

MNRAS **502,** 4842–4857 (2021) doi:10.1093/mnras/stab182
Advance Access publication 2021 January 25

A hot mini-Neptune in the radius valley orbiting solar analogue HD 110113

H. P. Osborn [1,2★] D. J. Armstrong [3,4] V. Adibekyan,[5] K. A. Collins,[6] E. Delgado-Mena,[5] S. B. Howell,[7] C. Hellier,[8] G. W. King [3,4] J. Lillo-Box [9] L. D. Nielsen [10] J. F. Otegi,[10] N. C. Santos,[5,11] C. Ziegler,[12] D. R. Anderson [3,4] C. Briceño,[13] C. Burke,[2] D. Bayliss [3,4] D. Barrado,[9] E. M. Bryant,[4,3] D. J. A. Brown [3,4] S. C. C. Barros,[5,11] F. Bouchy,[10] D. A. Caldwell,[14] D. M. Conti,[15] R. F. Díaz,[16] D. Dragomir,[17] M. Deleuil,[18] O. D. S. Demangeon,[5,11] C. Dorn,[19] T. Daylan,[2†] P. Figueira,[5,20] R. Helled,[19] S. Hoyer,[18] J. M. Jenkins,[7] E. L. N. Jensen,[21] D. W. Latham,[6] N. Law,[22] D. R. Louie,[23] A. W. Mann,[22] A. Osborn [3,4] D. L. Pollacco,[4] D. R. Rodriguez,[24] B. V. Rackham [2,25] G. Ricker,[2] N. J. Scott,[7] S. G. Sousa [5] S. Seager,[2,25] K. G. Stassun [26] J. C. Smith,[14] P. Strøm,[3,4] S. Udry,[10] J. Villaseñor,[2] R. Vanderspek,[2] R. West [3,4] P. J. Wheatley [3,4] and J. N. Winn[27]

Affiliations are listed at the end of the paper

Accepted 2021 January 7. Received 2020 December 21; in original form 2020 November 7

ABSTRACT

We report the discovery of HD 110113 b (*TESS* object of interest-755.01), a transiting mini-Neptune exoplanet on a 2.5-d orbit around the solar-analogue HD 110113 ($T_{\rm eff}$ = 5730 K). Using *TESS* photometry and High Accuracy Radial velocity Planet Searcher (HARPS) radial velocities gathered by the *NCORES* program, we find that HD 110113 b has a radius of 2.05 ± 0.12 $R_\oplus$ and a mass of 4.55 ± 0.62 $M_\oplus$. The resulting density of $2.90^{+0.75}_{-0.59}$ g cm^{-3} is significantly lower than would be expected from a pure-rock world; therefore HD 110113 b must be a mini-Neptune with a significant volatile atmosphere. The high incident flux places it within the so-called radius valley; however, HD 110113 b was able to hold on to a substantial (0.1–1 per cent) H–He atmosphere over its ∼4 Gyr lifetime. Through a novel simultaneous Gaussian process fit to multiple activity indicators, we were also able to fit for the strong stellar rotation signal with period 20.8 ± 1.2 d from the RVs and confirm an additional non-transiting planet, HD 110113 c, which has a mass of 10.5 ± 1.2 $M_\oplus$ and a period of $6.744^{+0.008}_{-0.009}$ d.

Key words: planets and satellites: detection – stars: individual: HD110113.

1 INTRODUCTION

Since its launch in 2018, NASA's *TESS* mission has attempted to detect small transiting planets around bright, nearby stars amenable to confirmation with radial velocity observations (Ricker et al. 2016). The HARPS spectrograph on the 3.6 m telescope at La Silla, Chile (Mayor et al. 2003) has been deeply involved in this follow-up effort, beginning with its first detection, the hot super-Earth Pi Mensae c (Huang et al. 2018), and continuing with the first multi-planet system *TESS* object of interest (TOI-125 Quinn et al. 2019; Nielsen et al. 2020),

This unique combination of space-based photometry (which provides planetary radius) and precise radial velocities (which provide planetary mass) also allows for the determination of exoplanet densities, and therefore an insight into the internal structure of worlds outside our Solar system. These analyses have revealed a diversity of planet structures in the regime between Earth and Neptune, from high-density evaporated giant planet cores like TOI-849b (5.2 g cm^{-3}; Armstrong et al. 2020), to low-density mini-Neptunes such as TOI-421 c (Carleo et al. 2020), as well as planets which follow a more linear track from rocky super-earths to Neptunes dominated by gaseous envelopes, such as the two inner planets orbiting ν^2 Lupi (Kane et al. 2020) and TOI-735 (Cloutier et al. 2020; Nowak et al. 2020).

The detection of exoplanets with well-constrained physical parameters can also lead to the discovery of statistical trends within the planet population, which encode information on planetary formation and evolution. The 'valley' seen around 1.8 $R_\oplus$ in Kepler data (Fulton et al. 2017; Van Eylen et al. 2018) is one such feature. According to current theory planets that first formed with gaseous envelopes within this valley have, due to heating from either their stars (e.g. evaporation, Owen & Wu 2017) or from internal sources (e.g. core-powered mass loss, Ginzburg, Schlichting & Sari 2018), lost those initial gaseous envelopes, thereby evolving to significantly smaller radii to become 'evaporated cores'. By observing the physical parameters of small, hot exoplanets, the exact mechanisms of this process can be revealed.

In this paper, we present the detection, confirmation, and RV characterization of two exoplanets orbiting the star HD 110113 – the hot mini-Neptune HD 110113 b and the non-transiting HD 110113 c. The observations from which these planets were detected are described in Section 2, while the analysis of that data is described in Section 3. In

★ E-mail: hugh.osborn@space.unibe.ch
† Kavli Fellow.

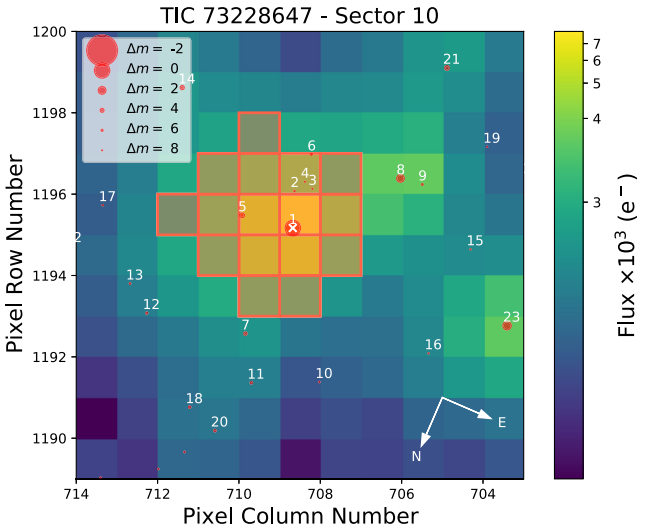

Figure 1. *TESS* photometric aperture plotted with `tpfplotter` (Aller et al. 2020). The default TESS aperture used by SAP is overplotted in red, and nearby stars down to Δmag = 8 from Gaia DR2 (Brown et al. 2018) are plotted as red circles. The target HD 110113 is marked with a white cross.

Section 4, we discuss the validity of the outer planet RV signal (4.1), whether HD 110113 is a solar analogue (4.2), the internal structure and evaporation of planet b (4.3 & 4.4), and potential future observations of the system (4.5). We summarize our conclusions in Section 5.

2 OBSERVATIONS

2.1 *TESS* photometry

HD 110113 was observed during *TESS* sector 10 with 2-min cadence for 22.5 d, excluding a 2.5-d gap between *TESS* orbits to downlink data. The light curve was extracted using the Science Processing Operations Centre (SPOC; Jenkins et al. 2016), simple aperture photometry (SAP) pipeline. It was then processed using the Pre-Search Data Conditioning (PDC; Smith et al. 2012; Stumpe et al. 2012, 2014) pipeline, producing precise detrended photometry with typical precision of 150 ppm/h for this star, and then searched for exoplanetary candidates with the Transiting Planet Search (TPS; Jenkins et al. 2010). This identified a strong candidate with a period of 2.54 d, a depth of only 410 ppm and a signal-to-noise ratio (SNR) of 7.6. Automated and human vetting subsequently designated this candidate a planet candidate and it was assigned TOI 755.01.

We inspected the *TESS* aperture using `tpfplotter` (plotted in Fig. 1; Aller et al. 2020) to ensure no nearby contaminant stars could be causing the transit. We found five stars within the aperture with contrast less than 8 mag, with the brightest with a Δmag of only 3.5. However, to cause the observed 410 ppm transit, this star would need to host eclipses of at least 1 per cent. Furthermore, being more than 1.2 pix, and therefore almost one full width half maximum (FWHM) of the point spread function (PSF), away from the target star, we would expect to see a significant centroid shift. However, the SPOC data validation modelling (Twicken et al. 2018; Li et al. 2019) shows no such shift and suggests the transit occurs within 0.25 pixels from the target position.[1] The other stars present are also >1 pixel away, and are increasingly fainter (Δmag of 6.9–7.9), requiring eclipse depths of 25–75 per cent. Causing the observed transit with such a blend scenario therefore becomes increasingly unlikely given the flat-bottomed transit shape of TOI-755.01. We conclude that a blend scenario from a known contaminant is unlikely, however, we pursue additional photometry to confirm.

[1]As shown by the SPOC DV report accessed at https://mast.stsci.edu/api/v0.1/Download/file/?uri=mast:TESS/product/tess2019085221934-s0010-s0010-0000000073228647-00212_dvr.pdf.

2.2 Ground-based photometric follow-up

We observed a full transit of TOI-755.01 continuously for 443 min in Pan-STARSS z-short band on UTC 2020 March 13 from the Las Cumbres Observatory Global Telescope (LCOGT; Brown et al. 2013) 1-m network node at Cerro Tololo Inter-American Observatory. The 4096 × 4096 LCOGT SINISTRO cameras have an image scale of 0.″389 per pixel, resulting in a 26 arcmin × 26 arcmin field of view. The images were calibrated by the standard LCOGT `BANZAI` pipeline (McCully et al. 2018). Photometric data were extracted using ASTROIMAGEJ (Collins et al. 2017). The mean stellar PSF in the image sequence had an FWHM of 2.″8. Circular apertures with radius 3.″1 were used to extract the differential photometry.

The TOI-755 SPOC pipeline transit depth of 397 ppm is too shallow to reliably detect with ground-based observations, so we instead checked for possible nearby eclipsing binaries (NEBs) that could be contaminating the irregularly shaped SPOC aperture that generally extends $\sim$1′ from the target star. To account for possible contamination from the wings of neighbouring star PSFs, we searched for NEBs out to 2.′5 from the target star. If fully blended in the SPOC aperture, a neighbouring star that is fainter than the target star by 8.54 mag in TESS-band could produce the SPOC-reported flux deficit at mid-transit (assuming a 100 per cent eclipse). To account for possible delta-magnitude differences between TESS-band and Pan-STARSS z-short band, we searched an extra 0.5 mag fainter (down to *TESS*-band magnitude 18.5).

The brightness and distance limits resulted in a search for NEBs in 90 Gaia DR2 stars, which includes all stars marked in red in Fig. 1 and a further 67 contaminants with Δmag > 8. We estimated the expected NEB depth in each neighbouring star by taking into account both the difference in magnitude relative to TOI-755 and the distance to TOI-755 (to account for the estimated fraction of the star's flux that would be contaminating the TOI-755 SPOC aperture). If the root mean squared (RMS) scatter of the 10-min binned light curve of a neighbouring star is more than a factor of three smaller than the expected NEB depth, we consider an NEB to be tentatively ruled out in the star over the observing window. We then visually inspect each neighbouring star's light curve to ensure no obvious eclipse-like signal. The LCOGT data rule out possible contaminating NEBs at the SPOC pipeline nominal ephemeris and over a -1.7σ to $+2.3\sigma$ ephemeris uncertainty window. By process of elimination, we conclude that the transit is indeed occurring in TOI-755, or a star so close to TOI-755 that it was not detected by Gaia DR2, or the event occurred outside our observing window.

2.3 Ground-based archival photometry

Although detecting the transits of HD 110113 b required precise space-based photometry, ground-based photometric surveys have observed HD 110113 and can provide constraints on stellar variability, and therefore an independent measure of the stellar rotation period.

WASP-South was a wide-field array of eight cameras forming the Southern station of the "Wide-Angle Search for Planets" (WASP) transit-search survey (Pollacco et al. 2006). The field of HD 110113

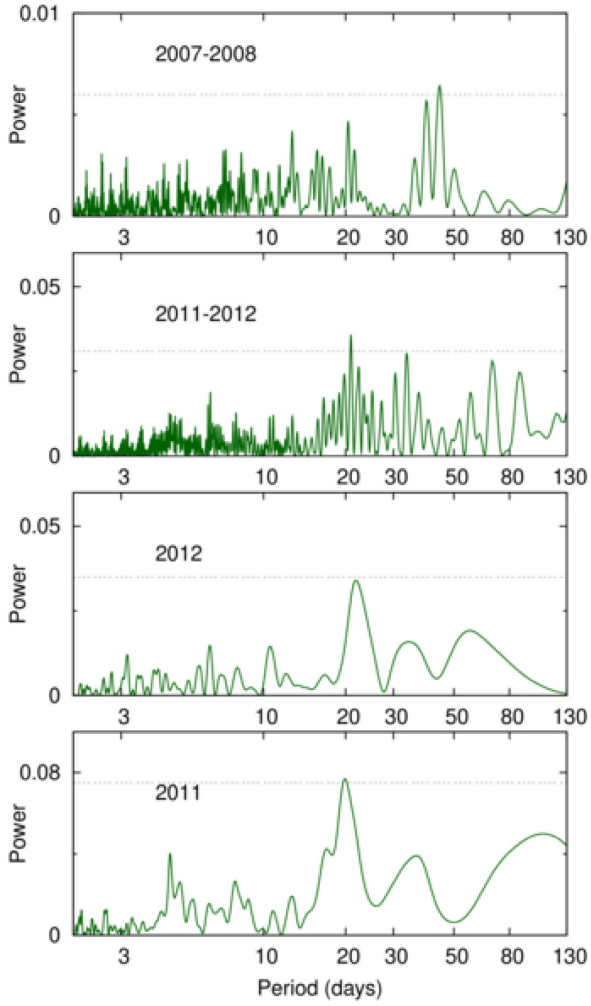

Figure 2. Periodograms of the WASP-South data for TOI-755. The top panel shows data from 2007 to 2008 combined, with a significant 42-d periodicity. The lower panels show data from 2011 to 2012, separately and combined, which show more strongly a periodicity of 21 d. The dotted horizontal lines are the estimated 1 per cent-likelihood false-alarm levels.

was observed over 150-night spans in each of 2007 and 2008, and then again over 2011 and 2012, acquiring a total of 30 000 photometric data points. WASP-South was at that time equipped with 200 mm, f/1.8 lenses, observing with a 400–700 nm passband, and with a photometric extraction aperture of 48 arcsecs. There are other stars in the aperture around HD 110113, but the brightest has $\Delta\text{mag} = 3$, while the others have $\Delta\text{mag} > 5$. Therefore, any rotation signal is likely from HD 110113. We searched the data for rotational modulations using the methods from Maxted et al. (2011).

The data from 2011 and 2012 show a modulation at a period of 21 ± 2 d (see Fig. 2). This is significant at the 1 per cent false-alarm level with an amplitude of 2 mmag, both in each year separately, and when the data from the 2 yr are combined. The data from 2007 and 2008 combined show a significant modulation at twice this period of $\sim 42 \pm 4$ d. There is also power near 21 d in the 2007/2008 periodogram, but it is not significant in its own right. Although it would seem more likely from these data alone that the rotational period of HD 110113 is 42 ± 4 d, with the 21-d period coming from the first harmonic, the WASP data cannot on its own distinguish between these two possible periods.

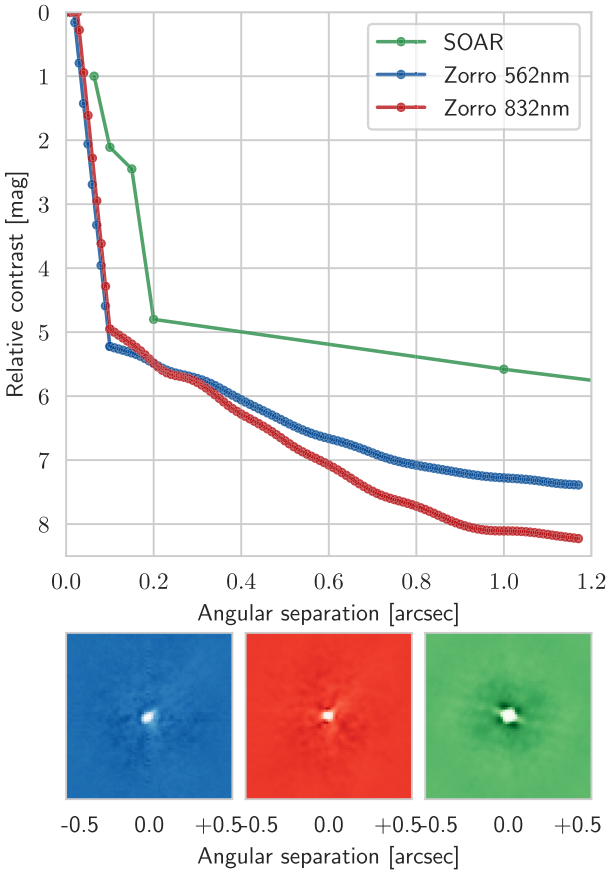

Figure 3. Contrast curves and images from Gemini/Zorro (blue & red for 562 and 832 nm, respectively), and SOAR (green).

2.4 High-resolution imaging

High-angular-resolution imaging is needed to search for nearby sources that can contaminate the *TESS* photometry, resulting in an underestimated planetary radius, or that can be the source of astrophysical false positives, such as background eclipsing binaries. Through the *TESS* Follow-Up Program, three such images were obtained across two telescopes, with the results shown in Fig. 3.

2.4.1 SOAR

We searched for stellar companions to TOI-755 with speckle imaging on the 4.1-m Southern Astrophysical Research (SOAR) telescope (Tokovinin 2018) on 2019 July 14 UT, observing in Cousins I-band, a similar visible bandpass as *TESS*. More details of the observation are available in Ziegler et al. (2020). The 5σ detection sensitivity and speckle auto-correlation functions from the observations are shown in Fig. 3. No nearby stars with magnitudes brighter than $I = 16$ were detected within $3''$ of HD 110113 in the SOAR observations.

2.4.2 Gemini/Zorro

High-resolution speckle interferometric images of HD 110113 were obtained on 2020 January 14 UT using the Zorro instrument mounted on the 8-m Gemini South telescope located on the summit of Cerro Pachon in Chile. Zorro simultaneously observes in two bands, (832 & 562 nm with widths of 40 & 54 nm, respectively), obtaining diffraction-limited images with inner working angles 0.017 and 0.028 arcsec, respectively. The observation consisted of 3-min sets of

1000 × 0.06-s images. All the images were combined and subjected to Fourier analysis, leading to the production of final data products, including speckle reconstructed imagery (see Howell et al. 2011). Fig. 3 shows the 5σ contrast curves in both filters for the Zorro observation and includes an inset showing the 832 nm reconstructed image. The resulting contrast limits reveal that HD 110113 is a single star to contrast limits of 5–8 mag, ruling out most main sequence companions to the star within the spatial limits of ∼11–320 au (for $d = 106.3$ pc).

2.5 HARPS high-resolution spectroscopy

Over the course of two observing seasons in 2018 and 2019, a total of 114 high-resolution spectra were taken with the High Accuracy Radial velocity Planet Searcher (HARPS, Pepe et al. 2002; Mayor et al. 2003) on the ESO 3.4 m telescope at La Silla, Chile. These spectra were taken as part of the *NCORES* program (PI:Armstrong, 1102.C-0249) designed to specifically study the internal structure of hot worlds.

We used the high-accuracy mode of HARPS with a 1″ science fibre on the star and a second on-sky fibre monitoring the background flux during exposure. The nominal exposure time was 1800 s, with a few exceptions of slightly longer or shorter integration, depending on observing conditions and schedule.

Spectra and Radial Velocity (RV) information were extracted using the offline HARPS data reduction pipeline hosted at Geneva Observatory. We use a flux template matching a G1 star to correct the continuum-slope in each echelle order. The spectra were cross correlated with a binary G2 mask to derive the cross correlation function (CCF; Baranne et al. 1996), on which we fit a Gaussian function to obtain RVs, FWHM, and contrast. Additionally, we compute the bisector-span (Queloz et al. 2001) of the CCF and spectral indices tracing chromospheric activity (Boisse et al. 2009; Gomes da Silva et al. 2011).

We reach a typical SNR per pixel of 75 (order 60, 631 nm) in individual spectra, corresponding to an RV error of 1.41 m s^{-1}. The HARPS spectra and derived RVs were accessed and downloaded through the DACE portal hosted at the University of Geneva (Buchschacher et al. 2015) under the target name HD 110113.[2]

3 ANALYSIS

3.1 Stellar parameters

3.1.1 Global stellar parameters

The star's effective temperature ($T_{\rm eff}$), surface gravity ($\log g$), and metallicity ([Fe/H]) were derived using a recent version of the MOOG code (Sneden 1973) and a set of plane-parallel ATLAS9 model atmospheres (Kurucz 1993). The analysis was done in local thermodynamic equilibrium (LTE). The methodology used is described in detail in Sousa et al. (2011) and Santos et al. (2013). The full spectroscopic analysis is based on the equivalent widths (EWs) of 233 Fe I and 34 Fe II weak lines by imposing ionization and excitation equilibrium. The line-list used was taken from Sousa et al. (2008). We obtained resulting parameters of $T_{\rm eff} = 5732 \pm 16$ K, $\log g = 4.46 \pm 0.05$, and [Fe/H] $= 0.14 \pm 0.02$. To account for potential systematic uncertainties, we increased the error bars to 50 K and 0.05 dex for $T_{\rm eff}$ and $\log g$, respectively.

[2]https://dace.unige.ch/radialVelocities/?pattern=HD110113

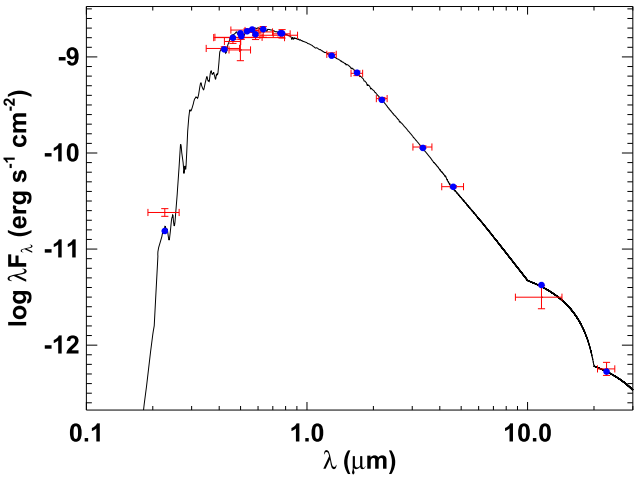

Figure 4. SED of HD 110113. Red symbols represent the observed photometric measurements, where the horizontal bars represent the effective width of the passband. Blue symbols are the model fluxes from the best-fitting Kurucz atmosphere model (black).

To constrain the physical stellar parameters of HD 110113 given the observed information, we applied three techniques.

The first technique was to use the main-sequence calibrations of Torres, Andersen & Giménez (2010), which derives $R_{\rm s}$ and $M_{\rm s}$ using polynomial functions of $T_{\rm eff}$, $\log g$, and [Fe/H], which are built using the observed properties of calibration stars. Uncertainties were propagated using 10 000 Monte Carlo draws and the mass was corrected using the calibration of Santos et al. (2013). This produced a mass and radius of 0.989 ± 0.01 M$_\odot$ and 0.998 ± 0.025 R$_\odot$, respectively, although Torres et al. (2010) suggest minimum uncertainties of 0.06 M$_\odot$ and 0.03 R$_\odot$, respectively.

The second was using theoretical isochrones ("Modules for Experiments in Stellar Astrophysics" Isochrones and Stellar Tracks - MIST; Choi et al. 2016) as well as observed properties (e.g. colours) to constrain stellar parameters, which we performed using ISOCLASSIFY (Huber 2017; Berger et al. 2020). Inputs included the derived spectral properties $T_{\rm eff}$, $\log g$, and [Fe/H], as well as archival data for HD 110113 including *APASS* B & V magnitudes (Henden et al. 2015), *Gaia* parallax, Gp, Rp, Bp, and luminosity (Brown et al. 2018), *SkyMapper* ugriz observations (Onken et al. 2019) and *2MASS* JHK observations (Skrutskie et al. 2006). This resulted in a mass & radius of $1.004^{+0.042}_{-0.047}$ M$_\odot$ and 1.002 ± 0.028 R$_\odot$, respectively. The well-constrained nature of the input measurements mean that we are limited by the gridsize of the theoretical isochrones, which despite an initial array of more than 3 million points, resulted in only 112 samples within all available constraints.

As a final independent determination of the basic stellar parameters for HD 110113, we performed an analysis of the broadband spectral energy distribution (SED) of the star together with the *Gaia* DR2 parallax (adjusted by +0.08 mas to account for the systematic offset reported by Stassun & Torres 2018), in order to determine an empirical measurement of the stellar radius, following the procedures described in Stassun & Torres (2016), Stassun, Collins & Gaudi (2017), and Stassun et al. (2018). We pulled the $B_T V_T$ magnitudes from *Tycho-2*, the *BVgri* magnitudes from *APASS*, the JHK_S magnitudes from *2MASS*, the W1–W4 magnitudes from *WISE*, the $GG_{\rm BP}G_{\rm RP}$ magnitudes from *Gaia*, and the NUV magnitude from *GALEX*. Together, the available photometry spans the full stellar SED over the wavelength range 0.2–22 μm (see Fig. 4).

Table 1. Stellar parameters.

Parameter	Value	Parameter	Value
TOI ID	TOI-755	RA [°]	190.036 5636[a]
TIC ID	73228647[b]	RA [hms]	12:40:08.78[a]
HD	HD 110113	Dec. [°]	−44.3120777[a]
HIP	HIP 61820	Dec. [dms]	−44:18:43.48[a]
Gaia ID	6133384959942131968[a]	δRA [mas yr^{-1}]	− 3.72 ± 0.1[a]
π (mas)	9.38 ± 0.036[a]	δDec. [mas yr^{-1}]	− 13.68 ± 0.12[a]
d (pc)	106.3 ± 0.72[e]	R_s [R$_\odot$]	0.968 ± 0.018[e]
B	10.71 ± 0.032[c]	M_s [M$_\odot$]	0.997 ± 0.06[e]
V	10.063 ± 0.027[c]	log g	4.46 ± 0.05[e]
Gaia G	9.91 ± 0.0004[a]	$T_{\rm eff}$ [K]	5732 ± 50[e]
TESS mag	9.4628 ± 0.006[b]	[Fe/H]	0.14 ± 0.02[e]
J[d]	8.903 ± 0.037[c]	$v \sin i$ [km s^{-1}]	1.74 ± 0.15[e]
H[d]	8.594 ± 0.063[c]	$P_{\rm rot}$ [d]	20.8 ± 1.2[f]
K[d]	8.502 ± 0.024[c]	Age [Gyr]	4.0 ± 0.5 Gyr[g]

[a]From Gaia DR2 (Brown et al. 2018). [b]From the *TESS* Input Catalogue v8 (Stassun et al. 2019). [c]Johnson magnitudes from APASS (Henden et al. 2015). [d]From 2MASS (Skrutskie et al. 2006). [e]Derived from HARPS spectra and archival data – see Section 3.1.1. [f]Determined using the GP fit to activity indicators and RVs as described in 3.2.1. [g]Derived from [Y/Al] abundance–age relation as described in Section 3.1.2.

We performed a fit using Kurucz stellar atmosphere models, with the $T_{\rm eff}$, [Fe/H], and log g adopted from the spectroscopic analysis. The only additional free parameter is the extinction (A_V), which we restricted to the maximum line of sight value from the dust maps of Schlegel, Finkbeiner & Davis (1998). The resulting fit is very good (Fig. 4) with a reduced χ^2 of 1.4 and best-fitting $A_V = 0.03 \pm 0.03$. Integrating the (unreddened) model SED gives the bolometric flux at Earth, $F_{\rm bol} = 2.597 \pm 0.091 \times 10^{-9}$ erg s^{-1} cm^{-2}. Taking the $F_{\rm bol}$ and $T_{\rm eff}$ together with the *Gaia* DR2 parallax gives the stellar radius, $R_\star = 0.968 \pm 0.018$ R$_\odot$. In addition, we can use the $R_\star$ together with the spectroscopic log g to obtain an empirical mass estimate of $M_\star = 0.99 \pm 0.08$ M$_\odot$.

Taken together, all the stellar parameters as derived above are consistent, and all suggest that HD 110113 is a solar analogue with mass and radius very close to the Sun. As the SED radius measurement is least affected by sample size or systematic uncertainty, we assume this as a final radius. Similarly, the mass obtained from the log g and the SED-derived $R_\star$ (0.99 ± 0.08 M$_\odot$) is nearly identical to that from the MR relationship (0.989 ± 0.01 M$_\odot$), suggesting they converge on the same value. We therefore use the mass as defined from the offset-corrected Torres et al. (2010) calibrations, with the uncertainty inflated to reflect the typical systematic error (0.06 M$_\odot$).

To compute the $v \sin i$ from the FWHM, we used the relations of Dos Santos et al. (2016), who studied the HARPS spectra of a large number of solar twins. We used this to first estimate the $v_{\rm macro}$ from the $T_{\rm eff}$ and log g derived in Section 3.1.1 (3.64 ± 0.1 km s^{-1}), and then combined this with the measured FWHM to estimate a $v \sin i$ of 1.74 ± 0.15 km s^{-1}, although the uncertainties here may be underestimated due to systematic uncertainties. Using the calculated R_s, this corresponds to a maximum rotation period ($P_{\rm max}$) of 28 ± 3 d, assuming an aligned system.

Derived stellar parameters are shown in Table 1.

3.1.2 *Chemical abundances*

Stellar abundances of the elements were also derived using the same tools and models as for stellar parameter determination as well as using the classical curve-of-growth analysis method assuming LTE. Although the EWs of the spectral lines were automatically measured with ARES, for the elements with only two to three lines available, we performed careful visual inspection of the EWs measurements. For the derivation of chemical abundances of refractory elements, we closely followed the methods described in the literature (e.g. Adibekyan et al. 2012, 2015; Delgado Mena et al. 2014, 2017). Abundances of the volatile elements, O and C, were derived following the method of Delgado Mena et al. (2010) and Bertran de Lis et al. (2015). Since the two spectral lines of oxygen are usually weak and the 6300.3 Å line is blended with Ni and CN lines, the EWs of these lines were manually measured with the task `splot` in IRAF. Lithium and sulfur abundances were derived by performing spectral synthesis with MOOG, following the works by Delgado Mena et al. (2014) and Costa Silva, Delgado Mena & Tsantaki (2020), respectively. Both abundance indicators are very similar to the solar values. All the [X/H] ratios are obtained by doing a differential analysis with respect to a high S/N solar (Vesta) spectrum from HARPS. The stellar parameters and abundances of the elements are presented in Table 2.

Table 2. Derived stellar abundances. [Y/X]-based ages using the 3D formula of Delgado Mena et al. (2019; table 10: age & $a + b \times T_{\rm eff} + c \times$ [Fe/H] $+ d \times$ [Y/Mg]).

Parameter	Value	Error
Abundances		
A(Li)	1.09	0.08
[Fe/H]	0.14	0.02
[S/H]	0.03	0.04
[Na/H]	0.141	0.038
[Mg/H]	0.129	0.021
[Al/H]	0.105	0.014
[Si/H]	0.097	0.022
[Ca/H]	0.092	0.062
[Ti/H]	0.140	0.030
[Cr/H]	0.156	0.032
[Ni/H]	0.130	0.024
[O/H]	− 0.012	0.083
[C/H]	0.032	0.012
[Cu/H]	0.116	0.016
[Zn/H]	0.050	0.012
[Sr/H]	0.170	0.073
[Y/H]	0.170	0.039
[Zr/H]	0.152	0.045
[Ba/H]	0.123	0.047
[Ce/H]	0.120	0.051
[Nd/H]	0.135	0.056
Derived abundance ratios		
Mg/Si	1.32	0.09
Fe/Si	1.08	0.07
Mg/Fe	1.23	0.08
Ages		
[Y/Mg] Age (Gyr)	4.09	0.75
[Y/Ti] Age (Gyr)	4.09	0.95
[Y/Zn] Age (Gyr)	3.29	0.77
[Y/Si] Age (Gyr)	3.95	0.86
[Y/Al] Age (Gyr)	4.00	0.54

We find that the [X/Fe] ratios of most elements are close to solar as expected for a star with this metallicity, whereas [O/Fe] and [C/Fe] are slightly subsolar, since these ratios tend to slightly decrease above solar metallicity (e.g. Bertran de Lis et al. 2015; Franchini et al. 2020). Moreover, we used the chemical abundances of some elements to derive ages through the so-called chemical clocks (i.e.

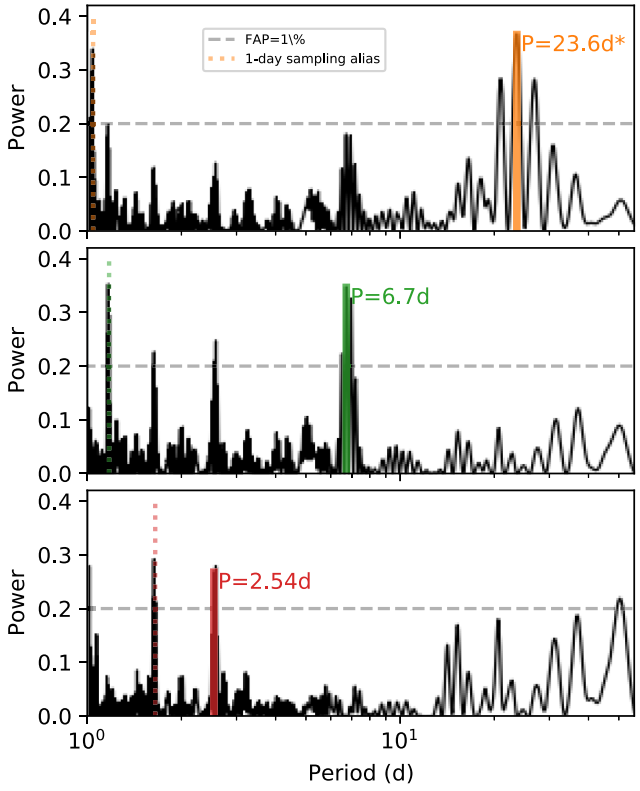

Figure 5. Periodograms of RVs after linear decorrelation with S-index and FWHM. The upper panel shows the raw periodogram, while subsequent panels show the periodogram after the removal of the previously marked peak. The 2.54-d peak is accompanied by a significant peak at the 1-d sampling alias (1.65 d), but the knowledge of a 2.54-d planet in the *TESS* photometry breaks this degeneracy. The remaining peaks in the final periodogram are likely due to sampling aliases associated with the ∼60-d span of observations.

certain chemical abundance ratios, which have a strong correlation with age). We applied the 3D formulas described in Delgado Mena et al. (2019), which also consider the variation in age produced by the effective temperature and iron abundance. The chemical clocks [Y/Mg], [Y/Zn], [Y/Ti], [Y/Si], and [Y/Al] were derived. We selected the [Y/Al] age, 4.0 ± 0.5 Gyr, as the representative age, as it is consistent with all others and has the smallest uncertainty.

3.2 Combined modelling of RV & photometry

3.2.1 Treatment of radial velocities

All activity indicators showed clear signs of stellar variability, likely due to the presence of starspots. To remove this stellar activity, we first turned to linear decorrelation of the RV signal using activity indicators. The FWHM and S-index showed the clearest rotational signals, so we selected these and used the decorrelation technique provided with the DACE spectroscopy PYTHON package (Buchschacher et al. 2015).[3] Despite this decorrelation removing much of the stellar variability signal, the peak at ∼22 d remained the single strongest signal in the radial velocity time series (see Fig. 5). To remove the rotation signal at 23.68 ± 0.08 d, we fitted a 5-parameter Keplerian model (with eccentricity e, argument of periastron Ω, & semi-amplitude K as free parameters, with period P and time of transit t_0 constrained from the periodogram). The next strongest signals were at 6.73 ± 0.03 and 2.541 ± 0.0008 d with amplitudes of 3.88 ± 0.31 and 2.55 ± 0.31 m s^{-1}, respectively. This was followed by signals on longer periods, which are most likely spurious due to rotational and observational aliases.

Although this linear decorrelation and Keplerian-fitted rotation period was able to reveal the planetary RV signals, stellar variability cannot in general be modelled as a Keplerian. Instead, we turned to a Gaussian process (GP) to model the impact of rotation on the RVs. GPs have frequently been used in the analysis of radial velocities affected by activity (e.g. Haywood et al. 2014; Dumusque et al. 2019). One GP kernel well-suited to stellar rotation is a mix of simple harmonic oscillator (SHO) terms corresponding to $P_{\rm rot}$ and $P_{\rm rot}/2$, which we built using EXOPLANET and CELERITE packages.[4]

In order to limit the impact of the GP on the planetary RV signal, we fitted activity indicators and RV time series simultaneously with the same GP kernel, as these should follow the same underlying variations with the exception of planetary reflex motion. A similar approach was previously used by Grunblatt, Howard & Haywood (2015) to model stellar variability in the Kepler-78b system, and by Suárez Mascareño et al. (2020) to find an outer candidate orbiting Proxima Centauri. By explicitly linking the variation found across activity indicators and RVs, this method has the same effect as 'training' a GP on an activity indicator (e.g. Dumusque et al. 2019). However, it avoids having to run multiple models consecutively and transfer the output PDF of a training sample into a second model – a process which loses information intrinsic to the likely non-Gaussian distributions of the GP hyper-parameters as well as information about the correlations between parameters. This technique also enables the use of multiple time series. In this case, we chose S-index and FWHM to co-fit the covariance function with the RVs, as these showed the clearest rotation signal.

To achieve this, the hyper-parameters for rotation period, mix factor between $P_{\rm rot}$ and $P_{\rm rot}/2$ terms, signal quality (Q), and the difference in signal quality between modes (ΔQ) were kept constant between S-index, FWHM, and RV time series, while the signal amplitude and mean, which are not shared across parameters, were set as separate parameters. For each time series, we also used a jitter term to model noise not included by measurement errors and to prevent GP over-fitting. All hyper-parameters were given broad priors, although the rotation period was constrained to the value obtained from a Lomb–Scargle periodogram (Lomb 1976; Scargle 1982) with a standard deviation of 20 per cent. All parameter priors are listed in Table A1.

We also noted that the FWHM errors produced by the HARPS pipeline appeared over-estimated – more than twice the estimated error derived from the median absolute difference between measurements. Therefore, the FWHM errors were multiplied by a factor of 0.4386 such that the median error matched the point-to-point RMS as calculated from the median absolute difference.

While we used the GPs to model the covariance between points in each time series, a mean function is also required to calibrate the average value over time, which we applied separately to each of the three time series. A two-parameter (i.e. linear) trend term was included to model potential long-term drift in the RVs, although the resulting gradient was not significant (-0.14 ± 0.73 m s^{-1} d^{-1}). Single-parameter mean values were included to model the offset of S-index and FWHM from zero.

[3] https://dace.unige.ch/tutorials/?tutorialId=34

[4] We used the `exoplanet.gp.terms.RotationTerm` implementation.

3.2.2 Treatment of photometry

We downloaded the PDC_SAP light curve from the Mikulski Archive for Space Telescopes (MAST). As high-resolution imaging revealed no close stellar neighbours missed by e.g. the *TESS* input catalogue (Stassun et al. 2019), we made the assumption that the PDC-extracted and dilution-corrected light curve for this target was accurate.

We then normalised the PDC_SAP time series by its median and masked anomalous flux points from the time series by cutting data more than 4.2σ different from both preceding and succeeding neighbours.

We initially tried to use the same CELERITE GP kernel to predict both RV and photometric time-series deviations. This proved to not be possible, likely because the effect of stellar variability on photometry is not necessarily at the same timescale as for RVs (Aigrain, Pont & Zucker 2012). Similarly, although a Lomb–Scargle periodogram of the raw *TESS* light curve does show a peak with a period around 25 d, the processed PDC_SAP light curve is flat, likely as variability on the order of a *TESS* orbit (∼14 d) is removed during processing.

The remaining variability is therefore likely to be the result of stellar granulation, which is well-suited to be modelled with a single GP SHO kernel with quality $Q = 1/\sqrt{2}$ (Foreman-Mackey et al. 2017; Barros et al. 2020). To produce the initial hyperparameters (ω_0 & S_0) and priors for the combined analysis and reduce the possibility of the GPs attempting to model the transits themselves, we first fitted this GP to the photometry with planetary transits cut. The interpolated posterior distributions from this analysis then provided the priors for the combined analysis. A jitter term was also included to model the effect of high-frequency noise not fully encapsulated by the photon noise (e.g. stellar & spacecraft jitter).

We modelled the limb darkening using two approaches: one where limb darkening is a free parameter, reparametrized using the approach of Kipping (2013b) and fitted to the transit with uninformative priors that cover the physical parameter space; and another where the expected theoretical limb darkening parameters for the star as generated by Claret (2017) are used as priors for the analysis. We found the resulting distributions to be consistent, and chose to use the second, constrained approach in the final modelling. This used a normal prior with the mean, μ, set from the theoretical parameter and σ set as 0.1 which we chose instead of the uncertainty found when propagating the stellar parameters through the Claret (2017) relation, which was likely too constraining and did not account for systematic uncertainties. The radius ratio R_p/R_s was treated using the log amplitude to avoid negative values, and b was reparametrized with R_p/R_s following the EXOPLANET implementation of Espinoza (2018).

As ground-based photometry was not precise enough to observe a transit (see Section 2.2), we restrict this analysis to only the *TESS* photometry and HARPS spectroscopy.

3.2.3 Combined model

We modelled full Keplerian orbits for the two planets, with eccentricity priors according to the Kipping (2013a) beta distribution.

Monte Carlo sampling, while able to explore the parameter space around a best-fitting solution, does not deal well with exploring unconstrained parameters with multiple local minima. Therefore, in order to allow our model to explore a single solution, we included normal priors on period and t_0 using the values and uncertainties from the TOI catalogue in the case of the 2.54-d planet, and from the RV periodogram in the case of the 6.7-d planet. In all cases, we artificially inflated these uncertainties to make sure the parameters were not over-constrained by their priors, which is confirmed by noting that the posterior distributions are, in all cases, narrower than the priors.

Table 3. Derived planet properties. ⋆ The mass of planet c refers to the $M_p \sin i$. † Surface temperature assumes a uniform surface and an albedo of 0.2.

Parameter	HD 110113 b	HD 110113 c
Epoch, t_0 [BJD-2457000]	$1570.101^{+0.004}_{-0.005}$	1798.17 ± 0.19
Orbital period, P [d]	$2.541^{+0.0005}_{-0.001}$	$6.744^{+0.008}_{-0.009}$
Semi-major axis, a [AU]	0.035 ± 0.001	$0.068^{+0.001}_{-0.002}$
Orbital eccentricity, e	$0.093^{+0.079}_{-0.064}$	$0.045^{+0.079}_{-0.038}$
Argument of periastron, Ω	-0.47 ± 0.68	-0.1 ± 1.2
Radius ratio [R_p/R_s]	0.018 ± 0.001	–
Radius, R_p ($R_\oplus$)	2.05 ± 0.12	–
Impact parameter, b	0.31 ± 0.22	–
Transit duration, t_D [d]	$0.099^{+0.005}_{-0.007}$	–
RV semi-amplitude, K ($m\,s^{-1}$)	2.15 ± 0.28	3.58 ± 0.37
Planet mass, M_p ($M_\oplus$)	4.55 ± 0.62	10.5 ± 1.2 ⋆
Planet density, ρ_p ($g\,cm^{-3}$)	$2.90^{+0.75}_{-0.59}$	–
Insolation, S (kWm^{-2})	1001.0 ± 40.0	272.0 ± 11.0
Surface temperature, T_p (K)†	1371.0 ± 14.0	990.0 ± 10.0

The combined model, built using the EXOPLANET (Foreman-Mackey et al. 2020) package, was sampled using the No-U Turn Sampler in the Hamiltonian Monte Carlo PYMC back-end (Salvatier, Wiecki & Fonnesbeck 2016) using five independent chains with 2000 steps and an additional 500 steps burn-in. This produced 10 000 independent samples. Model priors and posteriors are displayed in Table A1.

The results from the combined model are shown in Tables 3 and A1, with the HARPS RV time series and best-fitting models shown in Fig. 6, phase-folded RVs and model shown in Fig. 7, and *TESS* photometry and best-fitting light curves shown in Fig. 8.

4 DISCUSSION

4.1 Evidence for HD 110113 c

The periodogram of the activity-corrected radial velocity time series showed a clear signal at 6.75 d, even stronger than that of the planet at 2.54 d (Fig. 5). No such signal was found by TESS' automatic TPS; however, there is a chance such a signal may have been missed. A search using the `transit least squares` algorithm (Hippke & Heller 2019) on the HD 110113 b-subtracted light curve found no signal around 6.7 d, and a visual inspection of the light curve around the likely epochs of transits (given the limits from the RV detection) reveals no candidate dips associated with an outer candidate. Indeed, when running a combined model of two transiting planets, with constraints on orbits from the RVs, the posteriors for the radius of the outer planet were $<0.64\,R_\oplus$ at $1-\sigma$ which, given the 10.5 ± 1.2 $M_\oplus$ mass of HD 110113 c, would be physically impossible, even with an iron-core. Therefore, we come to the conclusion that HD 110113 c is likely non-transiting.

In order to assess whether the RV signal alone warrants calling HD 110113 c a confirmed planet or merely a candidate, we ran two combined models with identical priors and with one model including a non-transiting planet around 6.7 d. We then burned-in each model for 500 samples and ran the `find_MAP` function in `PyMC3` to find the maximum likelihood for each model, allowing us to compare the difference in Bayesian Information Criterion (ΔBIC) between the models. The resulting value of $\Delta\mathrm{BIC} = 16.32$ clearly favours a two-planet model over a single planet model, with $\Delta\mathrm{BIC} > 10$ suggesting 'very strong' evidence over the null hypothesis.

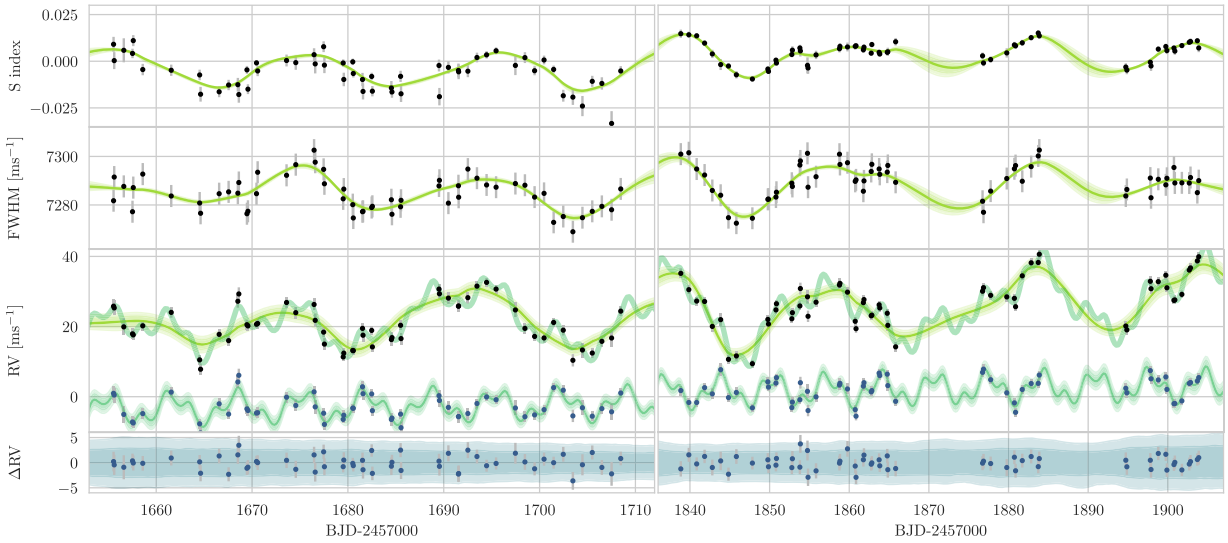

Figure 6. S-index, FWHM and RV time series of HD110113 for two seasons of HARPS monitoring, with GP models and 2σ uncertainty regions overplotted in green. Below the raw RV time series is the GP-removed RV time series, with the modelled planetary reflex motion and background trend (turquoise). At the very bottom, the full model residuals are shown, with an RMS of only 1.31 m s^{-1} – extremely close to the median HARPS measurement uncertainty (1.36 m s^{-1}).

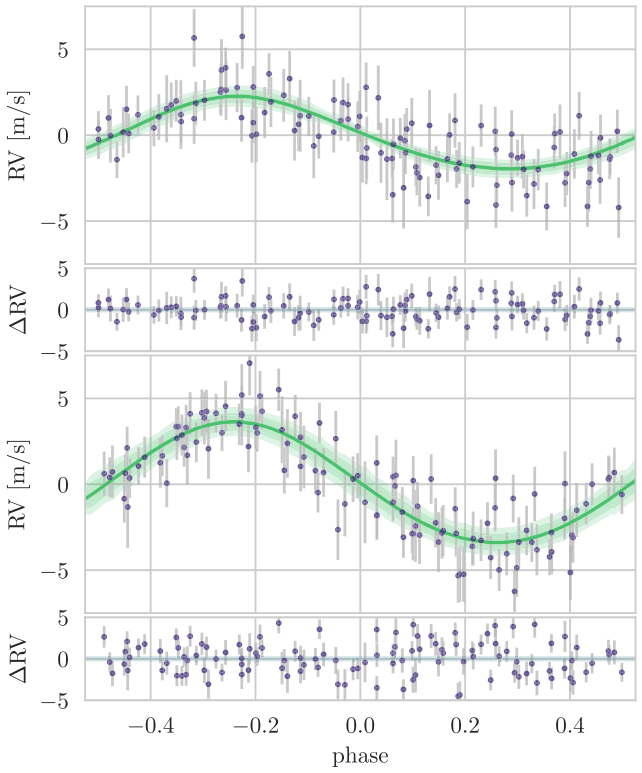

Figure 7. Phase-folded RVs (with the best-fitting GP model, linear trend, and the other planetary signal removed) for HD 110113 b (top) and HD 110113 c (bottom), with model-subtracted residuals.

Another test for the RV signal of HD 110113 c is the coherence of the signal over time, as radial velocity variation due to, e.g. stellar variability is not likely to remain coherent over multiple observing seasons. We verified these two ways using the decorrelated and rotation-subtracted radial velocities previously used to form RV periodograms (see Fig. 5). Firstly, we processed each season individually, finding that the signals at 2.451 and 6.75 d coincide with peaks during both seasons, albeit at lower signal strength. Next, we applied the Bayesian generalized Lomb–Scargle periodogram (BGLS; Mortier et al. 2015) to subsets of our RV time series to test signal coherence as per the technique of Mortier & Collier Cameron (2017). Fig. 9 shows that the signal of HD 110113 c passes this test – remaining evident even in data sets with only a handful of data points.

It should be noted that the period of HD 110113 c, at $6.744^{+0.008}_{-0.009}$ d, is close to the $P_{\rm rot}/3$ harmonic. However, there appears little evidence of a signal in the RV periodogram at $P_{\rm rot}/2$, so a large coherent signal at $P_{\rm rot}/3$ would be unexpected. However, it is possible that with certain inclinations and spot locations such harmonics may be boosted (Boisse et al. 2011; Vanderburg et al. 2016). Interestingly, the periodogram of the S-index data does show a strong peak at $P_{\rm rot}/2$ and a weaker peak at $P_{\rm rot}/3$, but this occurs at 7.25 d – significantly separated from the RV peak at $6.744^{+0.008}_{-0.009}$. While we confirm the presence of this second planet, as given ΔBIC > 10, the amplitude of the signal may be affected by the presence of a signal at $P_{\rm rot}/3$, therefore the mass of HD 110113 c should be treated as uncertain.

Multiple lines of evidence point to the signal of HD 110113 c being planetary in origin. Future RV measurements should help further disentangle stellar rotation and the signal amplitude, and may even reveal new candidates in this system.

The majority of short-period multiplanet systems are typically aligned with mutual inclinations of only a few degrees (Lissauer et al. 2011; Figueira et al. 2012; Winn & Fabrycky 2015). To investigate whether this could also be true for HD 110113, we used the derived impact parameter of planet b and the semimajor axial ratio of b & c to calculate the expected impact parameter of planet c in a perfectly co-planar scenario ($b_c = 0.60 \pm 0.42$) and the minimum mutual inclination ($\Delta i = 1.6^{+1.4}_{-1.6}{}^{\circ}$). Therefore, the HD 110113 planetary system is still consistent with an aligned planetary system.

Throughout this work, we quote $M_p \sin i$ for HD 110113 c. However, a clear non-detection of transits can constrain a planet's inclination, and therefore also reduce the lower limit on a planet's mass. However, in this case, the reduction in minimum mass caused by assuming $b > 1.0$ is smaller than 0.25 per cent. Therefore, including this factor would not significantly change the mass estimate from $M_p \sin i$. It is also worth noting that planets b & c have an orbital period ratio near 8/3, although harmonics beyond 2: 1 are highly unlikely to create measurable transit timing variations (Deck & Agol 2015).

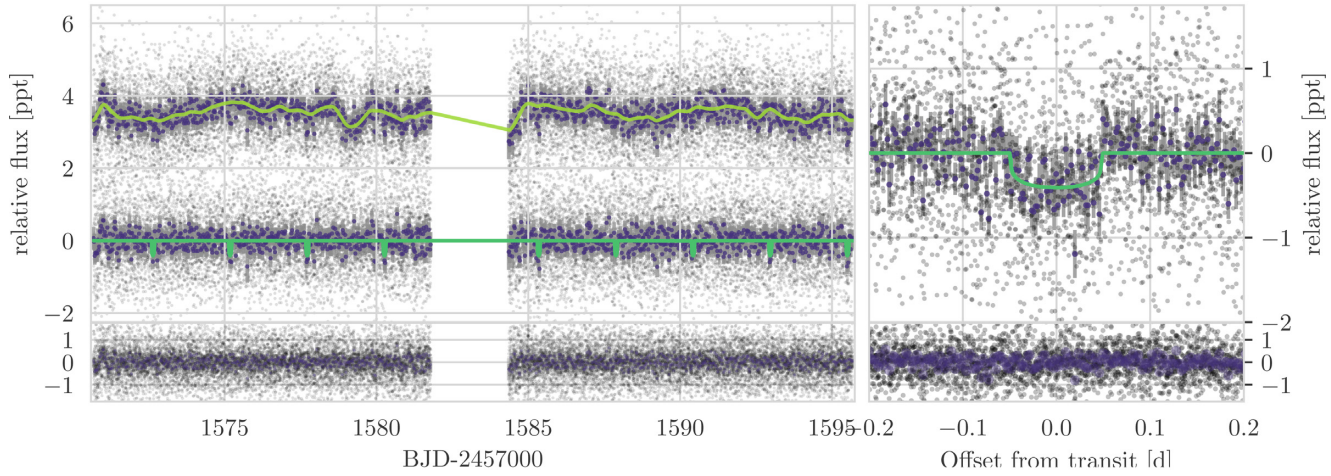

Figure 8. *TESS* photometry, where black dots represent individual 2-min cadence data and dark circles (with errorbars) represent 30-min bins. Upper left: *TESS* PDC_SAP time series with best-fitting GP model (both offset by 3.5ppt), and GP-subtracted light curve with the best-fitting transit model over-plotted (no offset). Lower left: residuals, with both GP model and transit models subtracted from the light curve. Upper right: phase-folded light curve of HD 110113 b zoomed to the transit. Lower right: phase-folded residuals.

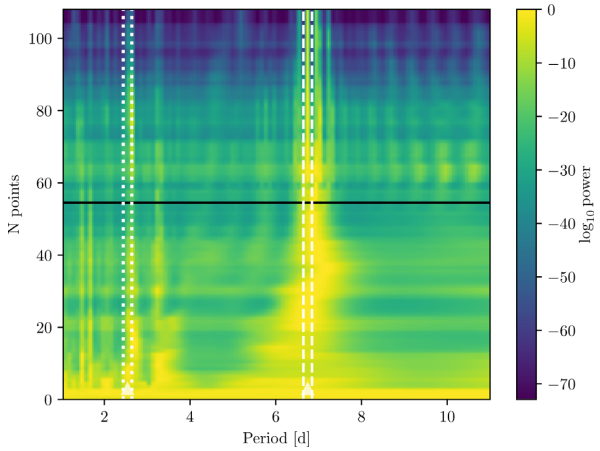

Figure 9. A 2D BGLS periodogram of HD 110113 radial velocities (after decorrelation and subtraction of the strongest rotation signal) performed on increasing numbers of radial velocity points, as proposed by Mortier & Collier Cameron (2017). Periods which maintain signal-strength and periodicity as a function of observation number suggest coherent (and therefore planetary) signals. The two white vertical bands show our modelled periods of each planet. The vertical bands seen are due to signal aliases in the second observing season due to the data gap, which is marked with a black horizontal line.

4.2 A solar analogue?

It is remarkable to note just how sun-like HD 110113 is, with a radius, $T_{\rm eff}$ and $\log g$ all within 1σ uncertainties of solar values, with the exception of its slightly higher metallicity ([Fe/H] $= 0.14 \pm 0.02$), and correspondingly lower C & O (see Table 2; e.g. Bertran de Lis et al. 2015; Franchini et al. 2020). We speculate that the higher metallicity may explain why HD 110113 was able to form close-in mini-Neptunes (Mulders et al. 2016; Bitsch & Battistini 2020), which do not exist in our Solar system.

HD 110113 is also nearly the same age as the Sun, as can be seen in both the Yttrium-based ages (Table 2), and from the rotation rate (∼22 d from archival photometry, spectroscopy time series, & $v \sin i$). Indeed, this rotation rate is marginally faster than the Sun (25–26.5 d when measured with HARPS-N and converted to sidereal period; Milbourne et al. 2019). This could be explained by the fact that HD 110113 is slightly younger, the Sun rotates slower than average (Robles et al. 2008), or the presence of short-period planets has tidally inhibited the slow-down of HD 110113, although the effect for such small planets is likely to be small (Bolmont et al. 2012).

Thanks to their similarities, HD 110113 and its planets could prove a useful comparison to the Sun and the Solar system in the future.

Table 4. Inferred interior structure properties of TOI-755b.

Constituent	With H–He [%]	With H_2O [%]	Four-layer [%]
$M_{\rm core}/M_{\rm total}$	47^{+26}_{-24}	8^{+7}_{-6}	25^{+28}_{-18}
$M_{\rm mantle}/M_{\rm total}$	53^{+23}_{-24}	17^{+11}_{-9}	36^{+31}_{-19}
$M_{\rm water}/M_{\rm total}$	–	73^{+10}_{-13}	38^{+31}_{-24}
$M_{\rm H–He}/M_{\rm total}$	$1.0^{+0.3}_{-0.5}$	–	$0.102^{+0.04}_{-0.03}$

4.3 Composition

To explore the composition of HD 110113 b, we performed four-layer interior structure modelling, using as inputs the mass and radius determined by our joint modelling of *TESS* photometry and HARPS RVs. We followed the method of Otegi, Bouchy & Helled (2020), which assumes a pure iron core, a silicate mantle, a non-gaseous water layer, and a H–He atmosphere. In order to quantify the degeneracy between the different interior parameters and produce posterior probability distributions, we use a generalized Bayesian inference analysis with a Nested Sampling scheme (e.g. Buchner et al. 2014). The interior parameters that are inferred include the masses of the pure-iron core, silicate mantle, water layer, and H–He atmosphere. The ratios of Fe/Si and Mg/Si found in stars is expected to be mirrored in the protoplanetary material, and therefore in the internal structures of exoplanets (Dorn et al. 2015). Hence, we use the values found by our stellar abundance analysis as a proxy for the core-to-mantle ratio. Given the observed molar ratio of Fe/Si (1.08 ± 0.07; Table 2) is higher than that of the Sun (0.85; Lodders, Palme & Gail 2009), we would expect planetary material around HD 110113 to be more iron-rich than Earth.

Table 4 lists the inferred mass fractions of the core, mantle, water-layer, and H–He atmosphere from the interior models. Due to

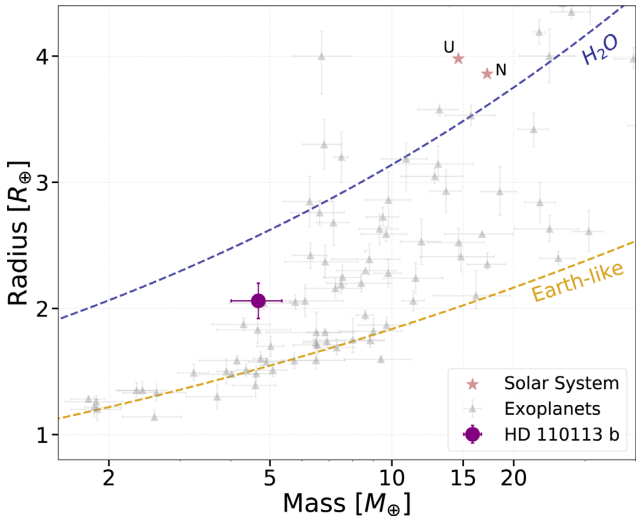

Figure 10. Mass–radius diagram of exoplanets with accurate mass and radius determination (Otegi et al. 2020). Also shown are the mass-radius relations for Earth-like and pure water compositions.

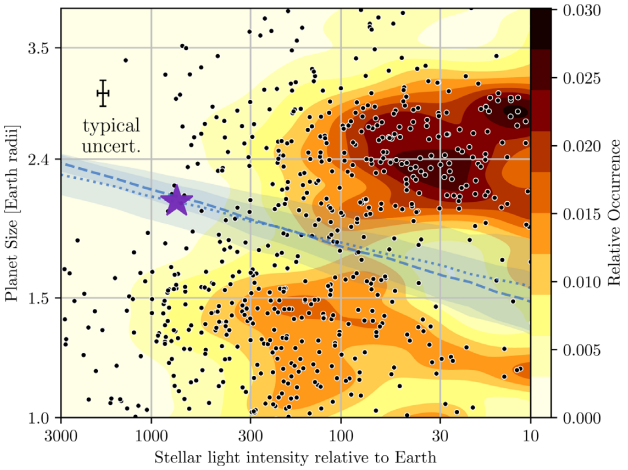

Figure 11. The distribution of Kepler planets by both insolation & planetary radius plot, with underlying occurrence distributions adapted from (Martinez et al. 2019). HD 110113 b is included as a purple star. The best-fitting positions of radius valleys from both (Martinez et al. (2019); dashed) and (Van Eylen et al. (2018); dotted) are plotted in blue, with conversion from period to insolation performed using the average stellar parameters in the Kepler samples. Typical uncertainties for both HD 110113 c and for the Kepler sample are shown in the top left.

the nature of the measurements, interior models cannot distinguish between water and H–He as the source of low-density material. Therefore, we ran both a four-layer model and two three-layer models, which leave out the H_2O and H–He envelopes, respectively. In the case of a H–He envelope, we find that the planet is only ∼1 per cent H–He by mass, with an iron-rich rocky interior making up 99 per cent of the planet. Any water present would likely decrease the core, mantle, & gaseous envelope fractions. However, a gas-free model would require 73^{+10}_{-13} per cent water. Such a high water-to-rock ratio is challenging from formation point of view. Therefore, HD 110113 b almost certainly has a significant gaseous envelope. Stars with super-solar metallicities are also less likely to host water-rich planets due to a higher C/O ratio (Bitsch & Battistini 2020), making a water-rich composition even less likely.

Fig. 10 shows the mass radius relation for Earth-like and pure water compositions (where the pure water line corresponds to a surface pressure of 1 bar, and without a water-vapor atmosphere). Also, shown are exoplanets with accurate mass and radius determinations from Otegi et al. (2020). The position of HD 110113 b makes it one of the lowest density worlds found with $M_p < 5\,M_\oplus$, and among a small class of low-density low-mass planets, which includes π Men c (Huang et al. 2018) and GJ 9827 b (Niraula et al. 2017).

4.4 Evaporation

With an insolation of 1001.0 ± 40.0 kW m^{-2} ($\sim 736\,S_\oplus$), it is extremely likely that HD 110113 b has been moulded by strong stellar radiation in some way. This is further suggested by placing HD 110113 b on the insolation-radius plots of Fulton et al. (2017) and Martinez et al. (2019), which clearly show the 'radius valley' (see Fig. 11). The negative slope of the valley with insolation means that, even with a radius of 2.05 ± 0.12 $R_\oplus$, HD 110113 b is positioned exactly within it.

Using both rotation and age, we predict a current X-ray luminosity (L_x/L_{bol}) of between 8.5×10^{-7} (with Prot; Wright et al. 2018) and 2.74×10^{-6} (with age; Jackson, Davis & Wheatley 2012). This implies total X-ray luminosities on the order of 3.3×10^{27} to 2.7×10^{28} erg and mass-loss rates (assuming an energy-limited regime) between 5×10^9 and 9×10^9 g s^{-1} (0.026– 0.05 $M_\oplus$ Gyr^{-1}). This is comparable to both GJ 436 b and Pi Men c under similar assumptions (King et al. 2019). Therefore, while it is currently highly irradiated, HD 110113 b is unlikely to currently be losing large quantities of its H–He atmosphere to space.

However, the integrated sum of mass-loss since the planet's formation is substantial, as young stars are typically far more active and far more X-ray luminous. We calculate that, assuming the current mass and radius, as much as 10 per cent of the planet's mass may have been lost through evaporation. The models of Zeng et al. (2019) suggest that a 1000 K planet with >5 per cent hydrogren and a 5.25 $M_\oplus$ core would have been >8.5 $R_\oplus$ in radius, suggesting that HD 110113 b potentially started as an extremely low-density Jupiter-radius world which was quickly stripped. How such a low-mass world came to possess such a large gaseous atmosphere raises more questions.

In any case, it is highly likely that HD 110113 b started with a thicker atmosphere of H–He, which, due to both evaporative and core-powered mass-loss, it lost much of over time. However, this is typically a runaway process: planets which lose the majority of their gas (i.e. those in the radius valley) typically lose it all (Owen & Wu 2017). Therefore the main unanswered question is: how did HD 110113 b escape becoming a naked core devoid of volatile envelope? Here, we propose two solutions to this:

(1) HD 110113 b started with a large envelope of H–He, perhaps as much as 10 per cent, which was gradually lost to evaporation and core-powered heating over time. But it had just enough gas to walk the tight-rope between keeping hold of a thick atmosphere and being completely stripped such that, at the point that evaporative forcing stopped, HD 110113 b still had ∼1 per cent of H–He by mass. The models of Rogers & Owen (2020; fig. 4) suggest that such a scenario is possible and may occur for planets that start gas-rich with around 4 per cent H–He.

(2) HD 110113 b did lose almost all of its H–He to evaporation and core-powered mass-loss. The current density is therefore explained by the planet having a large water content (e.g. an icy core), with potential out-gassing of a He-depleted secondary atmosphere contributing to the extended radius. Indeed, our composition calculations

include water in only solid & liquid states; therefore a thick steam (or supercritical; Mousis et al. 2020) H_2O atmosphere could reduce the density without requiring >50 per cent H_2O.

One final solution might be that HD 110113 b and HD 110113 c underwent late-stage migration to their current positions, thereby avoiding much of the evaporative forcing caused by the X-ray emissions of the young star. However, there is no theoretical mechanism in which a low-eccentricity two-planet system could undergo such late-stage migration long after the dispersal of the protoplanetary disc. Instead, multiplanet systems are capabale of undergoing early-stage migration damped by the protoplanetary gas disc (Cresswell & Nelson 2006; Carrera, Ford & Izidoro 2019), and massive single planets are thought capable of undergoing late-stage, high-eccentricity scattering on to shorter orbits (Ford & Rasio 2008; Beaugé & Nesvorný 2012). We therefore consider a solution through *in situ* processes more plausible than through migration.

These two predictions may be testable with future transmission spectroscopy observations, e.g. with *JWST* (Beichman et al. 2014; Greene et al. 2016).

4.5 Potential for future observations

The low-density nature of this hot mini-Neptune, combined with its bright host star, may enable transmission spectroscopy observations. Such measurement could test the hypotheses noted above, and search for a low-molecular weight primary atmosphere dominated by H–He, or a high molecular weight secondary atmosphere dominated by an overabundance of water vapour (Bean, Raymond & Owen 2021). To test this, we computed the emission and transmission spectroscopy metrics from Kempton et al. (2018).

We find that, among small planets with $R_p < 4\ R_\oplus$ (Akeson et al. 2013),[5] HD 110113 b ranks in the top 3 per cent most amenable for emission and the top 5 per cent for transmission spectroscopy with *JWST*. Although, when compared to one of the most favourable *JWST* targets: the low-density mini-Neptune GJ 1214 b, HD 110113 b provides only around 10 per cent the SNR in both transmission & emission – as is expected when comparing with a planet whose transits are 36 times deeper.

HD 110113 b will be also re-observed by *TESS* during Sector 37,[6] and could also be observed by ESA's *CHEOPS* telescope (Benz et al. 2020), both of which would improve the radius precision below the currently measured value of 7 per cent, thereby improving our knowledge of the internal structure of HD 110113 b.

5 CONCLUSION

We have presented the detection and confirmation of HD 110113 b, which was initially spotted as TOI-755.01 in *TESS* with an SNR of only 7.6σ and transit depth of 410 ppm. This marks one of the lowest SNR signals yet to be confirmed from *TESS*, and is testament to the unique ability of *TESS* to find planet candidates around bright stars, which can be redetected and characterized through independent RV campaigns.

High-resolution imaging and ground-based photometry rules out the presence of nearby companions and potential NEBs, thereby limiting the number of false-positives and giving us confidence to follow such a low-SNR signal. Our subsequent HARPS campaign obtained more than 100 HARPS spectra in order to characterize both HD 110113 b and its bright ($G = 9.9$ mag) star.

Analysis of these spectra revealed HD 110113 to be a Sun-like G-type star with slightly super-solar metallicity, but solar $T_{\rm eff}$, log g, and age. The RV time series also revealed strong activity on HD 110113 with a rotation period of 20.8 ± 1.2 d – a timescale corroborated by archival WASP photometry.

Removing this rotation period using both linear decorrelation and a co-fitted GP using S-index and FWHM activity indicators revealed the presence of two Keplerian signals, at $2.541^{+0.0005}_{-0.001}$ and $6.744^{+0.008}_{-0.009}$ d. The inner signal, from a planet with mass 4.55 ± 0.62 $M_\oplus$, corresponded to the detected *TESS* candidate with a radius, as modelled from the *TESS* photometry, of 2.05 ± 0.12 $R_\oplus$. The outer signal, from a planet with $M_p \sin i$ of 10.5 ± 1.2 $M_\oplus$ did not correspond to any transit events in the *TESS* light curve, and therefore is likely non-transiting. We were able to confirm it as a planet through Bayesian model comparison, which showed ΔBIC =16.32 in favour of a two-planet model.

The estimated density of HD 110113 b is $2.90^{+0.75}_{-0.59}$ g cm^{-3} – far lower than would be expected from a rocky core. By modelling four potential constituents – an iron core, silicate mantle, water ocean, and H–He atmosphere – we were able to rule out a gasless composition for HD 110113 b, suggesting that it has between 0.07 and 1.5 per cent H–He by mass. This is surprising given HD 110113 b's position in the 'radius valley' between gaseous mini-Neptunes and rocky super-Earths, and we suggest two possibilities for this unexpectedly low density: either HD 110113 b has a water-rich core and secondary atmosphere, or it began with a thick H–He envelope and managed to retain a small fraction of it despite significant evaporation and/or heating. Follow-up spectroscopy observations with the next generation of telescopes may reveal the answer, as well as far more about this interesting system.

ACKNOWLEDGEMENTS

We thank Raphaëlle Haywood, Maximillian Günther and FB for discussion on disentangling RV activity from signals.

This paper includes data collected by the *TESS* mission. Funding for the *TESS* mission is provided by the NASA Explorer Program and NASA's Science Mission directorate. We acknowledge the use of public *TESS* Alert data from pipelines at the *TESS* Science Office and at the *TESS* Science Processing Operations Center. This paper includes data collected by the *TESS* mission, which are publicly available from the Mikulski Archive for Space Telescopes (MAST).

This research has made use of the Exoplanet Follow-up Observation Program website, which is operated by the California Institute of Technology, under contract with the National Aeronautics and Space Administration under the Exoplanet Exploration Program.

Resources supporting this work were provided by the NASA High-End Computing (HEC) Program through the NASA Advanced Supercomputing (NAS) Division at Ames Research Center for the production of the SPOC data products.

This study is based on observations collected at the European Southern Observatory under ESO programme 1102.C-0249.

We thank the Swiss National Science Foundation (SNSF) and the Geneva University for their continuous support to our planet search programs. This work has been in particular carried out in the frame of the National Centre for Competence in Research *PlanetS* supported by the Swiss National Science Foundation (SNSF).

This publication makes use of The Data & Analysis Center for Exoplanets (DACE), which is a facility based at the University

[5] https://exoplanetarchive.ipac.caltech.edu/cgi-bin/nstedAPI/nph-nstedAPI?table=exoplanets&select=*&format=csv, accessed 2020 October 18.
[6] https://heasarc.gsfc.nasa.gov/cgi-bin/tess/webtess/wtv.py?Entry=73228647

of Geneva (CH) dedicated to extrasolar planets data visualization, exchange, and analysis. DACE is a platform of the Swiss National Centre of Competence in Research (NCCR) PlanetS, federating the Swiss expertise in Exoplanet research. The DACE platform is available at https://dace.unige.ch.

This work makes use of observations from the LCOGT network.

(Some of the) Observations in the paper made use of the High-Resolution Imaging instrument(s) 'Alopeke (and/or Zorro). 'Alopeke (and/or Zorro) was funded by the NASA Exoplanet Exploration Program and built at the NASA Ames Research Center by SBH, NJS, Elliott P. Horch, and Emmett Quigley. Data were reduced using a software pipeline originally written by Elliott Horch and Mark Everett. 'Alopeke (and/or Zorro) was mounted on the Gemini North (and/or South) telescope of the international Gemini Observatory, a program of NSF's Optical-Infrared Astronomy Research (NOIR) Lab, which is managed by the Association of Universities for Research in Astronomy (AURA) under a cooperative agreement with the National Science Foundation. on behalf of the Gemini partnership: the National Science Foundation (USA), National Research Council (Canada), Agencia Nacional de Investigación y Desarrollo (Chile), Ministerio de Ciencia, Tecnología e Innovación (Argentina), Ministério da Ciência, Tecnologia, Inovações e Comunicações (Brazil), and Korea Astronomy and Space Science Institute (Republic of Korea).

Based in part on observations obtained at the SOAR telescope, which is a joint project of the Ministério da Ciência, Tecnologia e Inovações (MCTI/LNA) do Brasil, the US National Science Foundation's NOIRLab, the University of North Carolina at Chapel Hill (UNC), and Michigan State University (MSU) and the international Gemini Observatory, a program of NSF's NOIRLab, which is managed by the Association of Universities for Research in Astronomy (AURA) under a cooperative agreement with the National Science Foundation. on behalf of the Gemini Observatory partnership: the National Science Foundation (USA), National Research Council (Canada), Agencia Nacional de Investigación y Desarrollo (Chile), Ministerio de Ciencia, Tecnología e Innovación (Argentina), Ministério da Ciência, Tecnologia, Inovações e Comunicações (Brazil), and Korea Astronomy and Space Science Institute (Republic of Korea).

HPO acknowledges support from NCCR/Planet-S via the CHESS fellowship.

DJA acknowledges support from the STFC via an Ernest Rutherford Fellowship (ST/R00384X/1).

VA, ED-M, NCS, ODSD, and SCCB acknowledge support by FCT - Fundação para a Ciência e a Tecnologia (Portugal) through national funds and by FEDER through COMPETE2020 - Programa Operacional Competitividade e Internacionalização by these grants: UID/FIS/04434/2019; UIDB/04434/2020; UIDP/04434/2020; PTDC/FIS-AST/32113/2017 & POCI-01-0145-FEDER-032113; PTDC/FIS-AST/28953/2017 & POCI-01-0145-FEDER-028953.

VA and EDM further acknowledge the support from FCT through Investigador FCT contracts IF/00650/2015/CP1273/CT0001 and IF/00849/2015/CP1273/CT0003.

ODSD and SCCB are supported through Investigador contract (DL 57/2016/CP1364/CT0004) funded by FCT.

JL-B is supported by the Spanish State Research Agency (AEI) Projects No. ESP2017-87676-C5-1-R and No. MDM-2017-0737 Unidad de Excelencia 'María de Maeztu'- Centro de Astrobiología (INTA-CSIC)

DD acknowledges support from the TESS Guest Investigator Program grant 80NSSC19K1727 and NASA Exoplanet Research P rogram grant 18-2XRP18_2-0136.

BVR thanks the Heising-Simons Foundation for support.

TD acknowledges support from MIT's Kavli Institute as a Kavli postdoctoral fellow

AO acknowledges support from an STFC studentship.

SH acknowledges CNES funding through the grant 837319

DJAB acknowledges support by the UK Space Agency.

This research made use of the following python software: EXOPLANET (Foreman-Mackey et al. 2020) and its dependencies (Astropy Collaboration 2013, 2018; Salvatier et al. 2016; Theano Development Team 2016; Foreman-Mackey et al. 2017, 2020; Foreman-Mackey 2018; Luger et al. 2019; Agol, Luger & Foreman-Mackey 2020); NUMPY (Harris et al. 2020); SCIPY (Virtanen et al. 2020); PANDAS (McKinney et al. 2011); ASTROPY (Robitaille et al. 2013); MATPLOTLIB (Hunter 2007); ASTROIMAGJ (Collins et al. 2017); TAPIR (Jensen 2013).

DATA AVAILABILITY

The data underlying this article are publicly available – *TESS* data are stored on the Mikulski Archive for Space Telescopes (MAST) at https://archive.stsci.edu/tess/, while HARPS data are both available on the Data & Analysis Center for Exoplanets (DACE) at https://dace.unige.ch/, and in Tables A2 and A3.

REFERENCES

Adibekyan V. Z., Sousa S. G., Santos N. C., Delgado Mena E., González Hernández J. I., Israelian G., Mayor M., Khachatryan G., 2012, A&A, 545, A32
Adibekyan V. et al., 2015, A&A, 583, A94
Agol E., Luger R., Foreman-Mackey D., 2020, AJ, 159, 123
Aigrain S., Pont F., Zucker S., 2012, MNRAS, 419, 3147
Akeson R. et al., 2013, PASP, 125, 989
Aller A., Lillo-Box J., Jones D., Miranda L. F., Barceló Forteza S., 2020, A&A, 635, A128
Armstrong D. J. et al., 2020, Nature, 583, 39
Astropy Collaboration, 2013, A&A, 558, A33
Astropy Collaboration, 2018, AJ, 156, 123
Baranne A. et al., 1996, A&AS, 119, 373
Barros S. C. C., Demangeon O., Díaz R. F., Cabrera J., Santos N. C., Faria J. P., Pereira F., 2020, A&A, 634, A75
Bean J. L., Raymond S. N., Owen J. E., 2021, J. Geophys. Res., 126, e06639
Beaugé C., Nesvorný D., 2012, ApJ, 751, 119
Beichman C. et al., 2014, PASP, 126, 1134
Benz W. et al., 2020, Experimental Astronomy, preprint (arXiv:2009.11633)
Berger T. A., Huber D., van Saders J. L., Gaidos E., Tayar J., Kraus A. L., 2020, AJ, 159, 280
Bertran de Lis S., Delgado Mena E., Adibekyan V. Z., Santos N. C., Sousa S. G., 2015, A&A, 576, A89
Bitsch B., Battistini C., 2020, A&A, 633, A10
Boisse I. et al., 2009, A&A, 495, 959
Boisse I., Bouchy F., Hébrard G., Bonfils X., Santos N., Vauclair S., 2011, A&A, 528, A4
Bolmont E., Raymond S. N., Leconte J., Matt S. P., 2012, A&A, 544, A124
Brown T. M. et al., 2013, PASP, 125, 1031
Brown A. et al., 2018, A&A, 616, A1
Buchner J. et al., 2014, A&A, 564, A125
Buchschacher N., Ségransan D., Udry S., Díaz R., 2015, in Taylor A. R., Rosolowsky E., eds, ASP Conf. Ser., Vol. 495, Astronomical Data Analysis Software an Systems XXIV (ADASS XXIV), Astron. Pac. Soc., San Francisco. p. 7
Carleo I. et al., 2020, AJ, 160, 114
Carrera D., Ford E. B., Izidoro A., 2019, MNRAS, 486, 3874
Choi J., Dotter A., Conroy C., Cantiello M., Paxton B., Johnson B. D., 2016, ApJ, 823, 102
Claret A., 2017, A&A, 600, A30

Cloutier R. et al., 2020, AJ, 160, 3
Collins K. A., Kielkopf J. F., Stassun K. G., Hessman F. V., 2017, AJ, 153, 77
Costa Silva A. R., Delgado Mena E., Tsantaki M., 2020, A&A, 634, A136
Cresswell P., Nelson R. P., 2006, A&A, 450, 833
Deck K. M., Agol E., 2015, ApJ, 802, 116
Delgado Mena E., Israelian G., González Hernández J. I., Bond J. C., Santos N. C., Udry S., Mayor M., 2010, ApJ, 725, 2349
Delgado Mena E. et al., 2014, A&A, 562, A92
Delgado Mena E., Tsantaki M., Adibekyan V. Z., Sousa S. G., Santos N. C., González Hernández J. I., Israelian G., 2017, A&A, 606, A94
Delgado Mena E. et al., 2019, A&A, 624, A78
Dorn C., Khan A., Heng K., Connolly J. A., Alibert Y., Benz W., Tackley P., 2015, A&A, 577, A83
Dos Santos L. A. et al., 2016, A&A, 592, A156
Dumusque X. et al., 2019, A&A, 627, A43
Espinoza N., 2018, Res. Notes Am. Astron. Soc., 2, 209
Figueira P. et al., 2012, A&A, 541, A139
Ford E. B., Rasio F. A., 2008, ApJ, 686, 621
Foreman-Mackey D., 2018, Res. Notes Am. Astron. Soc., 2, 31
Foreman-Mackey D., Agol E., Ambikasaran S., Angus R., 2017, AJ, 154, 220
Foreman-Mackey D., Luger R., Czekala I., Agol E., Price-Whelan A., Barclay T., 2020, exoplanet-dev/exoplanet v0.3.2. Available at: https://doi.org/10.5281/zenodo.1998447
Franchini M. et al., 2020, ApJ, 888, 55
Fulton B. J. et al., 2017, AJ, 154, 109
Ginzburg S., Schlichting H. E., Sari R., 2018, MNRAS, 476, 759
Gomes da Silva J., Santos N. C., Bonfils X., Delfosse X., Forveille T., Udry S., 2011, A&A, 534, A30
Greene T. P., Line M. R., Montero C., Fortney J. J., Lustig-Yaeger J., Luther K., 2016, ApJ, 817, 17
Grunblatt S. K., Howard A. W., Haywood R. D., 2015, ApJ, 808, 127
Harris C. R. et al., 2020, Nature, 585, 357
Haywood R. D. et al., 2014, MNRAS, 443, 2517
Henden A. A., Levine S., Terrell D., Welch D. L., 2015, in American Astronomical Society Meeting Abstracts, Vol. 225, p. 336.16
Hippke M., Heller R., 2019, A&A, 623, A39
Howell S. B., Everett M. E., Sherry W., Horch E., Ciardi D. R., 2011, AJ, 142, 19
Huang C. X. et al., 2018, ApJ, 868, L39
Huber D., 2017, Isoclassify: V1.2. Available at: http://doi.org/10.5281/zenodo.573372
Hunter J. D., 2007, Comput. Sci. Eng., 9, 90
Jackson A. P., Davis T. A., Wheatley P. J., 2012, MNRAS, 422, 2024
Jenkins J. M. et al., 2010, in Radziwill N. M., Bridger A., eds, SPIE Conf. Ser. Vol. 7740, Software and Cyber Infrastructure for Astronomy. SPIE, Bellingham, p. 77400D
Jenkins J. M. et al., 2016, in Chiozzi G., Guzman J. C., eds, SPIE Conf. Ser. Vol. 9913, Software and Cyberinfrastructure for Astronomy IV. SPIE, Bellingham, p. 99133E
Jensen E., 2013, Astrophysics Source Code Library, record ascl:1306.007
Kane S. R. et al., 2020, AJ, 160, 129
Kempton E. M.-R. et al., 2018, PASP, 130, 114401
King G. W., Wheatley P. J., Bourrier V., Ehrenreich D., 2019, MNRAS, 484, L49
Kipping D. M., 2013a, MNRAS, 434, L51
Kipping D. M., 2013b, MNRAS, 435, 2152
Kurucz R. L., 1993, SYNTHE Spectrum Synthesis Programs and Line Data. Cambridge Univ. Press, Cambridge
Li J., Tenenbaum P., Twicken J. D., Burke C. J., Jenkins J. M., Quintana E. V., Rowe J. F., Seader S. E., 2019, PASP, 131, 024506
Lissauer J. J. et al., 2011, ApJS, 197, 8
Lodders K., Palme H., Gail H.-P., 2009, Solar System. Springer, Berlin, p. 712
Lomb N. R., 1976, Ap&SS, 39, 447
Luger R., Agol E., Foreman-Mackey D., Fleming D. P., Lustig-Yaeger J., Deitrick R., 2019, AJ, 157, 64
McCully C., Volgenau N. H., Harbeck D.-R., Lister T. A., Saunders E. S., Turner M. L., Siiverd R. J., Bowman M., 2018, in Guzman J. C., Ibsen J., eds, Proc. SPIE Conf. Ser. Vol. 10707, Software and Cyberinfrastructure for Astronomy V. SPIE, Bellingham, p. 107070K
McKinney W. et al., 2011, Python for High Perform. Sci. Comput., 14, 1
Martinez C. F., Cunha K., Ghezzi L., Smith V. V., 2019, ApJ, 875, 29
Maxted P. F. L. et al., 2011, PASP, 123, 547
Mayor M. et al., 2003, The Messenger, 114, 20
Milbourne T. et al., 2019, ApJ, 874, 107
Mortier A., Collier Cameron A., 2017, A&A, 601, A110
Mortier A., Faria J. P., Correia C. M., Santerne A., Santos N. C., 2015, A&A, 573, A101
Mousis O., Deleuil M., Aguichine A., Marcq E., Naar J., Aguirre L. A., Brugger B., Goncalves T., 2020, ApJ, 896, L22
Mulders G. D., Pascucci I., Apai D., Frasca A., Molenda-Żakowicz J., 2016, AJ, 152, 187
Nielsen L. D. et al., 2020, MNRAS, 492, 5399
Niraula P. et al., 2017, AJ, 154, 266
Nowak G. et al., 2020, preprint (arXiv:2003.01140)
Onken C. A. et al., 2019, PASA, 36, e033
Otegi J., Bouchy F., Helled R., 2020, A&A, 634, A43
Owen J. E., Wu Y., 2017, ApJ, 847, 29
Pepe F. et al., 2002, The Messenger, 110, 9
Pollacco D. L. et al., 2006, PASP, 118, 1407
Queloz D. et al., 2001, A&A, 379, 279
Quinn S. N. et al., 2019, AJ, 158, 177
Ricker G. R. et al., 2016, Space Telescopes and Instrumentation 2016: Optical, Infrared, and Millimeter Wave. SPIE, Bellingham, p. 99042B
Robitaille T. P. et al., 2013, A&A, 558, A33
Robles J. A., Lineweaver C. H., Grether D., Flynn C., Egan C. A., Pracy M. B., Holmberg J., Gardner E., 2008, ApJ, 684, 691
Rogers J. G., Owen J. E., 2020, European Planetary Science Congress, EPSC2020–94
Salvatier J., Wiecki T. V., Fonnesbeck C., 2016, PeerJ Comput. Sci., 2, e55
Santos N. C. et al., 2013, A&A, 556, A150
Scargle J. D., 1982, ApJ, 263, 835
Schlegel D. J., Finkbeiner D. P., Davis M., 1998, ApJ, 500, 525
Skrutskie M. et al., 2006, AJ, 131, 1163
Smith J. C. et al., 2012, PASP, 124, 1000
Sneden C., 1973, ApJ, 184, 839
Sousa S. G. et al., 2008, A&A, 487, 373
Sousa S. G., Santos N. C., Israelian G., Mayor M., Udry S., 2011, A&A, 533, A141
Stassun K. G., Torres G., 2016, AJ, 152, 180
Stassun K. G., Torres G., 2018, ApJ, 862, 61
Stassun K. G., Collins K. A., Gaudi B. S., 2017, AJ, 153, 136
Stassun K. G., Corsaro E., Pepper J. A., Gaudi B. S., 2018, AJ, 155, 22
Stassun K. G. et al., 2019, AJ, 158, 138
Stumpe M. C. et al., 2012, PASP, 124, 985
Stumpe M. C., Smith J. C., Catanzarite J. H., Van Cleve J. E., Jenkins J. M., Twicken J. D., Girouard F. R., 2014, PASP, 126, 100
Suárez Mascareño A. et al., 2020, A&A, 639, A77
Theano Development Team, 2016, preprint (arXiv:1605.02688)
Tokovinin A., 2018, PASP, 130, 035002
Torres G., Andersen J., Giménez A., 2010, A&AR, 18, 67
Twicken J. D. et al., 2018, PASP, 130, 064502
Vanderburg A., Plavchan P., Johnson J. A., Ciardi D. R., Swift J., Kane S. R., 2016, MNRAS, 459, 3565
Van Eylen V., Agentoft C., Lundkvist M., Kjeldsen H., Owen J. E., Fulton B. J., Petigura E., Snellen I., 2018, MNRAS, 479, 4786
Virtanen P. et al., 2020, Nat. Methods, 17, 261
Winn J. N., Fabrycky D. C., 2015, ARA&A, 53, 409
Wright N. J., Newton E. R., Williams P. K., Drake J. J., Yadav R. K., 2018, MNRAS, 479, 2351
Zeng L. et al., 2019, Proc. Natl. Acad. Sci., 116, 9723
Ziegler C., Tokovinin A., Briceno C., Mang J., Law N., Mann A., 2020, in American Astronomical Society Meeting Abstracts, Vol. 235, p. 121.05

APPENDIX A: EXTRA TABLES

Table A1. List of free parameters used in the EXOPLANET combined analysis of the *TESS* light curve and HARPS radial velocities with their associated prior and posterior distributions.

Parameter	Prior	Posterior
Stellar parameters		
Stellar surface temperature, $T_{\rm eff}$ (K)	$\mathcal{N}(5732.0, 50.0)$	5732 ± 50
Stellar Mass, $M_{\rm s}$ ($M_\odot$)	$\mathcal{N}(0.9968, 0.06)$	0.997 ± 0.06
Stellar Radius, $R_{\rm s}$ ($R_\odot$)	$\mathcal{N}(0.968, 0.018)$	0.968 ± 0.018
Orbital parameters		
Transit Epoch, t_0 [BJD-2457000] b	$\mathcal{N}(1570.10189, 0.1)$	$1570.101^{+0.004}_{-0.005}$
Transit Epoch, t_0 [BJD-2457000] c	$\mathcal{N}(1798.1334, 1.0)$	1798.17 ± 0.19
Orbital Period, P [d] b	$\mathcal{N}_{\mathcal{U}}(2.540455, 0.002124, 2.35, 2.6)$	$2.541^{+0.0005}_{-0.001}$
Orbital Period, P [d] c	$\mathcal{N}_{\mathcal{U}}(6.7285, 0.05951, 6.65, 6.8)$	$6.744^{+0.008}_{-0.009}$
Orbital Eccentricity, e b	$\beta(0.867; 3.03)^a$	$0.093^{+0.079}_{-0.064}$
Orbital Eccentricity, e c	$\beta(0.867; 3.03)^a$	$0.045^{+0.079}_{-0.038}$
Argument of periastron, Ω b	$\mathcal{U}(-\pi, \pi)^b$	-0.47 ± 0.68
Argument of periastron, Ω c	$\mathcal{U}(-\pi, \pi)^b$	-0.1 ± 1.2
Photometric parameters		
log radius ratio [log $R_p/R_{\rm s}$] b	$\mathcal{U}(-11.513, -2.3023)$	-4.009 ± 0.063
Transit Impact Parameter b	$\mathcal{U}(0, 1 + R_p/R_s)^c$	0.31 ± 0.22
Quadratic Limb Darkening $a_{\rm LD}$	$\mathcal{N}_{\mathcal{U}}(0.367, 0.1, 0.0, 1.0)$	0.37 ± 0.1
Quadratic Limb Darkening $b_{\rm LD}$	$\mathcal{N}_{\mathcal{U}}(0.21, 0.1, 0.0, 1.0)$	$0.221^{+0.093}_{-0.096}$
Photometric jitter [log ppt]	$\mathcal{N}(0.7294, 5.0)$	$-8.0^{+1.7}_{-2.6}$
Photometric GP power	$\mathcal{I}(0.014, 0.006)^d$	0.012 ± 0.003
Photometric GP frequency (d^{-1})	$\mathcal{I}(3.525, 0.651)^d$	$3.73^{+0.48}_{-0.44}$
Photometric GP mean [ppt]	$\mathcal{I}(0.008, 0.036)^d$	$0.011^{+0.031}_{-0.035}$
HARPS parameters		
log RV semi-amplitude, log K b	$\mathcal{N}(0.3, 5.0)$	0.77 ± 0.13
log RV semi-amplitude, log K c	$\mathcal{N}(0.3, 5.0)$	1.27 ± 0.1
RV trend - intercept at BJD=2458779.717 ($m\,s^{-1}$)	$\mathcal{N}(0.0, 0.1)$	0.027 ± 0.01
RV trend - gradient ($m\,s^{-1}\,d^{-1}$)	$\mathcal{N}(0.0, 1.0)$	-0.24 ± 0.7
HARPS log jitter RV ($m\,s^{-1}$)	$\mathcal{N}(1.992, 5.0)$	$-0.5^{+0.7}_{-1.7}$
HARPS log jitter S index	$\mathcal{N}(6.527e-06, 5.0)$	$-12.84^{+0.53}_{-0.74}$
HARPS log jitter FWHM ($m\,s^{-1}$)	$\mathcal{N}(20.525, 5.0)$	0.1 ± 1.1
HARPS mean S-index	$\mathcal{N}(0.0, 0.00941)$	$-0.0^{+0.001}_{-0.002}$
HARPS mean FWHM ($m\,s^{-1}$)	$\mathcal{N}(7287.75, 7.5)$	7286.9 ± 1.1
HARPS GP log amplitude RV	$\mathcal{N}(2.984, 8.0)$	$3.66^{+0.35}_{-0.34}$
HARPS GP log amplitude S-index	$\mathcal{N}(-9.332, 8.0)$	$-9.64^{+0.37}_{-0.33}$
HARPS GP log amplitude FWHM	$\mathcal{N}(4.03, 8.0)$	3.77 ± 0.37
HARPS GP log rotation period, log $P_{\rm rot}$/log d	$\mathcal{N}_{\mathcal{U}}(3.024, 0.2, 1.099, 4.382)$	3.035 ± 0.06
HARPS GP log quality, Q	$\mathcal{N}(0.0, 10.0)$	$-1.1^{+1.6}_{-3.6}$
HARPS GP log quality differential, ΔQ	$\mathcal{N}(0.0, 5.0)$	$1.7^{+1.8}_{-1.4}$
HARPS GP $P_{\rm rot}$ - $P_{\rm rot}$/2 mix factor	$\mathcal{U}(0, 1)$	20.8 ± 1.2

Notes. $\mathcal{N}(\mu; \sigma^2)$ is a normal distribution with mean μ and width σ^2, $\mathcal{U}(a; b)$ is a uniform distribution between a and b, $\mathcal{N}_{\mathcal{U}}(\mu; \sigma^2, a, b)$ is a normal distribution with mean μ and width σ^2 multiplied with a uniform distribution between a and b, $\beta(a; b)$ is a Beta distribution with parameters a and b, and $\mathcal{I}(\mu; \sigma^2)$ is a distribution directly interpolated from the output of a pre-trained distribution with mean μ and standard deviation σ^2 (although the distribution may not follow a normal distribution). Posterior values and uncertainties represent the median and 1σ error boundaries. All other values (e.g. presented in Table 3) are directly determined from these fitted quantities. The prior uncertainties of input parameters t_0 and P were inflated from the input data uncertainties by factors of: $t_{0,\,b} = 23\times$, $t_{0,\,c} = 7\times$, $P_b = 3\times$, $P_c = 11\times$. [a]Described in Kipping (2013a). [b]Reparametrized in EXOPLANET to avoid discontinuities at $\pm\pi$. [c]EXOPLANET reparametrization of Espinoza (2018). [d]PYMC3Interpolation function of pre-trained GP.

Table A2. HARPS spectroscopy from first season (June–August 2019).

Time [BJD − 2457000]	RV [m s^{-1}]	σ_{RV}	S_{MW} –	σ_S	FWHM [m s^{-1}]	σ_{FWHM}
1655.5493	1.8	1.95	0.0091	0.004	7281.8	4.5
1655.6181	1.32	2.0	0.0003	0.0045	7291.5	4.5
1656.6167	− 4.08	2.39	0.0059	0.0064	7287.6	4.5
1657.5254	− 6.07	1.44	0.0042	0.0025	7277.2	4.5
1657.606	− 6.37	1.49	0.011	0.0029	7287.2	4.6
1658.5953	− 3.78	1.46	− 0.0045	0.0031	7292.7	4.6
1661.5662	0.04	1.48	− 0.0048	0.003	7283.7	4.5
1664.5324	− 13.5	1.36	− 0.0074	0.0028	7280.8	4.5
1664.6282	− 16.17	1.6	− 0.0177	0.004	7276.6	4.5
1666.5674	− 6.22	1.45	− 0.0164	0.0029	7284.6	4.5
1667.5542	− 8.01	1.39	− 0.0127	0.0028	7285.4	4.6
1668.5189	3.21	1.8	− 0.0126	0.0036	7284.8	4.5
1668.6197	5.3	1.88	− 0.0178	0.0044	7289.2	4.5
1669.466	− 3.47	1.32	− 0.0046	0.0021	7276.4	4.5
1669.5709	− 3.81	1.42	− 0.015	0.0026	7277.4	4.5
1670.4637	− 3.35	1.13	− 0.0009	0.0015	7284.6	4.5
1670.5832	− 3.13	1.46	− 0.0052	0.0028	7293.5	4.6
1673.5985	2.86	1.53	0.0004	0.0032	7292.2	4.6
1674.5613	− 0.04	1.69	− 0.0008	0.0038	7296.6	4.6
1676.4716	2.3	1.62	0.0035	0.0034	7302.6	4.6
1676.5886	− 2.22	1.88	− 0.0014	0.0051	7297.6	4.6
1677.4681	− 5.59	1.43	0.0078	0.0029	7294.7	4.6
1677.5491	− 9.0	1.68	− 0.0021	0.0043	7288.7	4.6
1679.5086	− 12.66	1.12	− 0.001	0.0019	7282.5	4.6
1679.571	− 11.58	1.56	− 0.0098	0.0036	7286.5	4.6
1680.5087	− 10.82	1.09	− 0.0003	0.0017	7280.1	4.6
1680.5634	− 10.88	1.16	− 0.0066	0.0021	7274.6	4.6
1681.5245	− 4.52	1.54	− 0.0098	0.0035	7277.2	4.5
1681.5771	− 6.48	1.75	− 0.0162	0.0043	7277.4	4.5
1682.4813	− 5.11	1.23	− 0.0081	0.002	7278.9	4.5
1682.5533	− 9.81	1.35	− 0.016	0.0028	7279.4	4.6
1684.5367	− 7.71	1.75	− 0.0143	0.0037	7282.2	4.5
1684.5971	− 7.15	1.49	− 0.0165	0.0031	7276.2	4.5
1685.4972	− 3.64	1.39	− 0.0081	0.003	7279.2	4.5
1685.5436	− 7.43	1.69	− 0.0174	0.0044	7281.9	4.6
1689.5056	6.68	1.47	− 0.0023	0.0032	7287.8	4.6
1689.5493	5.35	1.83	− 0.019	0.0047	7290.2	4.6
1690.4858	4.11	1.6	− 0.0033	0.0032	7280.8	4.5
1691.5335	1.79	1.58	− 0.005	0.0037	7287.9	4.6
1691.5549	1.87	1.62	− 0.0057	0.0039	7283.2	4.6
1692.5178	4.23	1.59	− 0.0053	0.0032	7294.8	4.5
1693.4664	7.52	1.36	0.002	0.0026	7291.0	4.5
1694.4709	8.59	1.19	0.0034	0.002	7288.2	4.5
1695.462	6.68	1.21	0.0056	0.0018	7287.3	4.5
1697.4761	0.74	2.07	− 0.0023	0.0052	7288.8	4.5
1698.4702	− 4.52	1.57	0.0019	0.0029	7288.1	4.5
1699.4797	− 6.82	1.3	− 0.0051	0.0024	7283.2	4.5
1700.4668	− 7.25	1.29	0.0007	0.0023	7284.8	4.5
1701.4669	− 2.83	1.19	− 0.0044	0.0021	7272.8	4.5
1702.4715	− 5.04	1.47	− 0.0185	0.0032	7275.2	4.5
1703.4744	− 13.62	1.76	− 0.0192	0.0042	7269.0	4.5
1704.4713	− 10.69	2.09	− 0.024	0.0054	7274.8	4.5
1705.4964	− 11.55	1.38	− 0.0108	0.0029	7277.4	4.5
1706.4982	− 8.22	1.47	− 0.0119	0.0033	7279.4	4.5
1707.5135	− 7.27	2.37	− 0.0333	0.0066	7278.0	4.5
1708.4678	0.39	1.35	− 0.0052	0.0026	7286.6	4.5

Table A3. HARPS spectroscopy from second season (Dec 2019–Feb 2020).

Time [BJD − 2457000]	RV [m s^{-1}]	σ_{RV}	S_{MW} –	σ_S	FWHM [m s^{-1}]	σ_{FWHM}
1838.8494	11.17	1.4	0.0147	0.0022	7301.0	4.5
1839.8578	6.52	1.26	0.0142	0.0017	7301.5	4.5
1840.8432	3.27	1.15	0.0136	0.0014	7294.8	4.5
1841.8384	3.16	1.19	0.0097	0.0015	7292.3	4.5
1842.8077	− 3.96	1.45	0.0039	0.0022	7286.0	4.5
1843.8559	− 2.03	1.74	− 0.0018	0.0029	7284.0	4.5
1844.8362	− 13.35	1.16	− 0.0026	0.0014	7274.8	4.5
1845.8271	− 12.38	1.33	− 0.0073	0.002	7272.5	4.5
1847.8389	− 14.59	1.11	− 0.0095	0.0012	7274.5	4.5
1849.7822	− 1.97	1.18	− 0.0042	0.0015	7282.3	4.5
1849.8576	− 3.28	1.13	− 0.0055	0.0013	7282.4	4.5
1850.7988	0.75	1.08	0.0006	0.0013	7283.3	4.5
1850.8597	2.51	1.04	− 0.001	0.0011	7285.2	4.5
1852.7908	− 1.78	1.17	0.0036	0.0015	7289.0	4.5
1852.8609	− 0.05	1.42	0.0059	0.0021	7287.6	4.5
1853.8015	1.87	1.25	0.0071	0.0017	7296.4	4.5
1853.8644	6.84	1.68	0.0055	0.003	7298.1	4.5
1854.757	4.48	1.88	− 0.0022	0.0043	7301.3	4.5
1854.8269	− 1.07	1.62	− 0.0036	0.0031	7287.3	4.5
1855.8321	2.95	1.38	0.0034	0.0022	7291.6	4.5
1858.775	7.83	1.33	0.0067	0.002	7300.9	4.5
1858.8351	8.32	1.31	0.0079	0.0018	7296.7	4.5
1859.7796	5.81	1.44	0.0076	0.0024	7297.4	4.5
1860.7517	− 2.5	1.26	0.008	0.0018	7289.7	4.5
1860.8525	− 4.61	1.19	0.0083	0.0015	7290.3	4.5
1861.7734	2.82	1.22	0.0061	0.0016	7285.7	4.5
1861.85	3.7	1.22	0.0075	0.0015	7289.9	4.5
1862.7588	− 0.94	1.1	0.0043	0.0012	7293.8	4.5
1862.8378	− 0.75	1.19	0.0089	0.0014	7296.8	4.5
1863.7554	2.21	1.13	0.0048	0.0014	7294.8	4.5
1863.8328	1.3	1.06	0.0039	0.0011	7292.6	4.5
1864.7737	− 0.21	1.25	0.0048	0.0017	7293.5	4.5
1864.8432	− 3.66	1.46	0.005	0.0022	7296.3	4.5
1865.8255	− 9.78	1.41	0.0104	0.002	7289.3	4.5
1876.7398	6.07	1.26	0.0029	0.0018	7281.5	4.5
1876.8589	7.09	1.32	− 0.0009	0.0018	7277.0	4.5
1877.7559	4.9	1.25	0.0009	0.0017	7285.7	4.5
1879.7785	4.46	1.56	0.0045	0.0025	7290.9	4.5
1880.7355	4.05	1.22	0.0087	0.0016	7294.9	4.5
1880.8847	1.67	1.22	0.0083	0.0017	7296.2	4.5
1881.7267	10.47	1.23	0.0099	0.0016	7289.8	4.5
1882.8435	14.18	1.23	0.0126	0.0015	7295.8	4.5
1883.7334	14.27	1.17	0.0151	0.0015	7300.2	4.5
1883.8645	16.62	1.26	0.0136	0.0017	7302.6	4.5
1894.7258	− 3.86	1.43	− 0.0031	0.0021	7283.7	4.5
1894.859	− 4.95	1.49	− 0.0048	0.0022	7286.4	4.5
1897.8044	8.9	1.29	− 0.0005	0.0017	7291.1	4.5
1897.8921	6.79	1.5	− 0.0025	0.0026	7283.0	4.5
1898.8055	8.8	1.18	0.0065	0.0014	7290.6	4.5
1899.7514	10.63	1.17	0.0079	0.0015	7288.3	4.5
1899.8854	7.06	1.2	0.0057	0.0019	7291.0	4.5
1900.7715	3.46	1.11	0.0071	0.0013	7295.4	4.5
1900.8838	3.59	1.21	0.0054	0.002	7289.1	4.5
1901.7655	5.17	1.07	0.0084	0.0012	7289.1	4.5
1902.6953	12.1	1.13	0.0102	0.0014	7289.0	4.5
1902.8507	12.72	1.16	0.0106	0.0017	7291.3	4.5
1903.7072	14.72	1.07	0.011	0.0012	7285.1	4.5
1903.885	15.9	1.26	0.0071	0.0022	7290.0	4.5

[1]*NCCR/PlanetS, Centre for Space & Habitability, University of Bern, Bern, CH-3012, Switzerland*
[2]*Department of Physics and Kavli Institute for Astrophysics and Space Research, Massachusetts Institute of Technology, Cambridge, MA 02139, USA*
[3]*Centre for Exoplanets and Habitability, University of Warwick, Gibbet Hill Road, Coventry CV4 7AL, UK*
[4]*Department of Physics, University of Warwick, Gibbet Hill Road, Coventry CV4 7AL, UK*
[5]*Instituto de Astrofísica e Ciências do Espaço, Universidade do Porto, CAUP, Rua das Estrelas, Porto 4150-762, Portugal*
[6]*Harvard-Smithsonian Center for Astrophysics, 60 Garden St, Cambridge, MA 02138, USA*
[7]*NASA Ames Research Center, Moffett Field, CA 94035, USA*
[8]*Astrophysics Group, Keele University, Staffs ST5 5BG, UK*
[9]*Centro de Astrobiologiía (CAB, CSIC-INTA), Dep. de Astrofísica, ESAC campus, Villanueva de la Cañada, Madrid E-28692, Spain*
[10]*Geneva Observatory, University of Geneva, Chemin des Mailettes 51, Versoix CH-1290, Switzerland*
[11]*Departamento de Física e Astronomia, Faculdade de Ciências, Universidade do Porto, Rua do Campo Alegre, Porto 4169-007, Portugal*
[12]*Dunlap Institute for Astronomy and Astrophysics, University of Toronto, 50 St. George Street, Toronto, Ontario M5S 3H4, Canada*
[13]*Cerro Tololo Inter-American Observatory, Casilla 603, La Serena, Chile*
[14]*SETI Institute 189 Bernardo Ave, Suite 200 Mountain View, CA 94043, USA*
[15]*American Association of Variable Star Observers, 49 Bay State Road, Cambridge, MA 02138, USA*
[16]*International Center for Advanced Studies (ICAS) and ICIFI (CONICET), ECyT-UNSAM, Campus Miguelete, 25 de Mayo y Francia, (1650) Buenos Aires, Argentina*
[17]*Department of Physics and Astronomy, University of New Mexico, 1919 Lomas Blvd NE, Albuquerque, NM 87131, USA*
[18]*Aix Marseille Univ, CNRS, CNES, LAM, 38 rue Frédéric Joliot-Curie, F-13388, Marseille, France*
[19]*Institute for Computational Science, University of Zurich,Winterthurerstr. 190, Zurich CH-8057, Switzerland*
[20]*European Southern Observatory, Alonso de Cordova 3107, Vitacura, Santiago, Chile*
[21]*Department of Physics & Astronomy, Swarthmore College, Swarthmore, PA 19081, USA*
[22]*Department of Physics and Astronomy, The University of North Carolina at Chapel Hill, Chapel Hill, NC 27599-3255, USA*
[23]*Department of Astronomy, University of Maryland, College Park, MD 20742, USA*
[24]*Space Telescope Science Institute, 3700 San Martin Drive, Baltimore, MD 21218, USA*
[25]*Department of Earth, Atmospheric and Planetary Sciences, Massachusetts Institute of Technology, Cambridge, MA 02139, USA*
[26]*Department of Physics & Astronomy, Vanderbilt University, 6301 Stevenson Center Ln., Nashville, TN 37235, USA*
[27]*Department of Astrophysical Sciences, Princeton University, 4 Ivy Lane, Princeton, NJ 08544, USA*

This paper has been typeset from a TEX/LATEX file prepared by the author.